The Impact of Moist Frontogenesis and Tropopause Undulation on the Intensity, Size, and Structural Changes of Hurricane Sandy (2012)

JUNG HOON SHIN AND DA-LIN ZHANG

Department of Atmospheric and Oceanic Science, University of Maryland, College Park, College Park, Maryland

(Manuscript received 7 December 2015, in final form 6 December 2016)

ABSTRACT

This study examines the relative roles of moist frontogenesis and tropopause undulation in determining the intensity, size, and structural changes of Hurricane Sandy using a high-resolution cloud-resolving model. A 138-h simulation reproduces Sandy's four distinct development stages: (i) rapid intensification, (ii) weakening, (iii) steady maximum surface wind but with large continued sea level pressure (SLP) falls, and (iv) reintensification. Results show typical correlations between intensity changes, sea surface temperature, and vertical wind shear during the first two stages. The large SLP falls during the last two stages are mostly caused by Sandy's northward movement into lower-tropopause regions associated with an eastward-propagating midlatitude trough, where the associated lower-stratospheric warm air wraps into the storm and its surrounding areas. The steady maximum surface wind occurs because of the widespread SLP falls with weak gradients lacking significant inward advection of absolute angular momentum (AAM). Meanwhile, three spiral frontogenetic zones and associated rainbands develop internally in the outer northeastern quadrant during the last three stages when Sandy's southeasterly warm current converges with an easterly cold current associated with an eastern Canadian high. Cyclonic inward advection of AAM along each frontal rainband accounts for the continued expansion of the tropical storm–force wind and structural changes, while deep convection in the eyewall and merging of the final two surviving frontogenetic zones generate a spiraling jet in Sandy's northwestern quadrant, leading to its reintensification prior to landfall. The authors conclude that a series of moist frontogenesis plays a more important role than the lower-stratospheric warmth in determining Sandy's size, intensity, and structural changes.

1. Introduction

Hurricane Sandy (2012) was one of the most destructive hurricanes: it produced about $50 billion (U.S. dollars) property damage and about 147 casualties. The storm has a record-breaking size in the extended best track—for example, with an averaged radius of the tropical storm–force wind of 660 km at 24 h prior to landfall at the New Jersey shoreline (Blake et al. 2013). The storm underwent several intensity changes with continuous size expansion as it moved from the southwestern Caribbean Sea to landfall at the New Jersey shoreline. Although Sandy's track and landfall were well predicted 5 days in advance (Blake et al. 2013; Magnusson et al. 2014), uncertainty remains concerning on the physical processes leading to the multiple intensity changes and the continued growth of the storm size during its life cycle as well as the timing of its extratropical transition (ET). Furthermore, it remains unclear about the roles of two upper-level troughs (i.e., a polar one and a subtropical one) and low-level baroclinicity in determining the reintensification of the storm prior to landfall.

Although there is not a universal definition of ET, the ET of a tropical cyclone (TC) often involves losing symmetric appearance, increasing radius of gale-force winds, increasing central sea level pressure (SLP), weakening or vertical tilting of a warm core, transformation from a warm to a cold core, and the appearance of a frontal structure under the influences of decreasing sea surface temperature (SST), and increasing vertical wind shear (VWS) and baroclinicity (Klein et al. 2000; Jones et al. 2003). Perhaps the most prominent structural change of an ET TC is the development of an extensive coverage of clouds and precipitation associated with warm frontogenesis when it interacts with low-level baroclinicity to the north (Harr and Elsberry 2000; Klein et al. 2000; Atallah and Bosart 2003; Colle 2003). After its warm core is replaced by a cold core, the TC may appear like an extratropical

Corresponding author e-mail: Da-Lin Zhang, dalin@umd.edu

DOI: 10.1175/JAS-D-15-0362.1

cyclone (Evans and Hart 2008). In some cases, the lower-tropospheric warm core could still be retained during ET (Browning et al. 1998; Thorncroft and Jones 2000; Evans and Hart 2003), which resembles a warm-core seclusion that is similar to that described in the conceptual model of Shapiro and Keyser (1990) for a mature extratropical cyclone (Galarneau et al. 2013). Reintensification of these systems, as often measured by central SLP drops, may occur in response to interaction with upper-level troughs (Harr and Elsberry 2000; Klein et al. 2000; Ritchie and Elsberry 2007). Despite the considerable research, our understanding of ET is still limited owing to the complex interaction between a warm-core TC and midlatitude baroclinic systems. In particular, few detailed observations are available over vast oceans, where most ET events take place, for understanding mesoscale processes leading to the intensity and structural changes of TCs during ET. See Jones et al. (2003) for a comprehensive review of the ET literature.

The objectives of this study are (i) to document the multiple intensity and structural changes of Hurricane Sandy (2012) from its rapid intensification (RI) over the Caribbean Sea to the subsequent weakening and reintensification prior to landfall and (ii) to examine different roles of low-level baroclinic processes, especially those occurring within its vortex circulation, and tropopause undulation in determining the intensity, size, and structural changes of the storm. The above objectives will be achieved mostly through a 138-h (0000 UTC 24 October–1800 UTC 29 October 2012) high-resolution, quadruply nested-grid simulation of the case using the Weather Research and Forecasting (WRF) Model, in addition to synoptic analysis. It should be mentioned that Galarneau et al. (2013) only studied Sandy's reintensification during its warm seclusion stage (i.e., after colder air encircles its warm core), and the subsequent landfall, using the WRF Model, initialized at 0000 UTC 28 October, with the finest grid size of 4 km. By applying the Sawyer–Eliassen equations to the model simulation, they found that Sandy's reintensification results primarily from the secondary circulation associated with frontogenesis as Sandy's vortex interacts with an approaching large-scale cold front.

The next section provides an overview of the structures and evolution of Sandy based on the National Hurricane Center (NHC) best-track data and the National Centers for Environmental Prediction (NCEP) final analysis. Section 3 describes the model configurations and validation of the numerical simulation. Section 4 shows the nonobservable structures and evolution of the storm and examines the different roles of lower- and upper-level processes in the intensity, structural, and size changes of Sandy using the 138-h model simulation. A summary and concluding remarks are given in the final section.

2. Overview

Hurricane Sandy (2012) originated in the Caribbean Sea on 22 October 2012. During the period of 24–26 October, Sandy moved nearly northward over a warm-SST region and made the first landfall in the eastern portion of Cuba around 0600 UTC 25 October (Fig. 1a). On 27–29 October the storm drifted northeastward slightly, which was 450 km to the east of the Gulf Stream. During this period, the underlying SST was about 2°–3°C colder than that earlier. Around 0600 UTC 29 October, Sandy recurved northwestward, and it made landfall along the New Jersey shoreline by 2330 UTC 29 October after moving across the Gulf Stream.

Figure 1b shows that at 0000 UTC 24 October, a cold front extended from north-central Canada to the central United States with a warm front stretched to the East Coast, and an eastern Canadian high was distributed from Hudson Bay southward to Bahamas. This implies that Sandy would be influenced by an approaching extratropical baroclinic system (Galarneau et al. 2013; Lackmann 2015), and a zonally distributed baroclinic zone with an easterly flow from the eastern Canadian high, after moving into the midlatitudes. Figure 2a shows that indeed Sandy, carrying high-equivalent potential temperature (θ_e) air of tropical origin, began to encounter an eastward-propagating upper-level trough with a vast low-θ_e air mass behind the surface cold front, and another low-θ_e air mass in eastern Canada, after moving northward to the east of Florida Peninsula at 0000 UTC 27 October; the leading edges of both air masses can be traced by $\theta_e = 310$ K at 900 hPa or height $z = 1$ km. The high (low)-θ_e air was cyclonically advected poleward (equatorward) in the eastern (western) semicircle regions of the storm; such a thermal pattern typically occurs during the ET of TCs (Harr and Elsberry 2000; Klein et al. 2000).

A vertical cross section through the upper-level trough and Sandy's core region, given in Fig. 2b, depicts a tropopause undulation that is similar to that discussed by Hirschberg and Fritsch (1991a). That is, the tropopause, as defined by 2 potential vorticity units (PVU; 1 PVU = 10^{-6} K kg^{-1} m^2 s^{-1}), became sharply lower across the two airmass interface to the northwest, with reversed horizontal potential temperature (θ) gradients in the trough region above 250 hPa. As will be seen in section 4, this relatively warmer air mass in the northwestern lower stratosphere played an important role in determining Sandy's structural and intensity

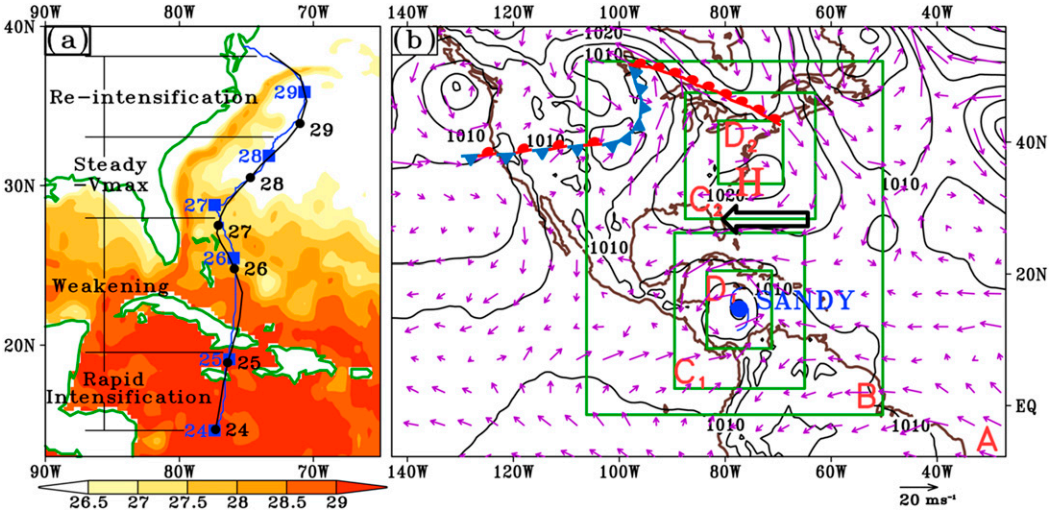

FIG. 1. (a) Comparison of the simulated track (blue) to the best track (black) of Hurricane Sandy during the period form 0000 UTC 24 Oct to 1800 UTC 29 Oct 2012, superimposed with the AVHRR-SST (shaded, °C) distribution. Four different stages of Sandy's life cycle are indicated here and in the rest of figures. (b) Model domain configuration, superimposed with SLP (contoured at 5-hPa intervals), 900-hPa wind vectors, and frontal distribution (plotted only over the eastern U.S. region) from the NCEP final analysis at 0000 UTC 24 Oct 2012. Domains A, B, C, and D have 45-, 15-, 5-, and 1.667-km resolutions, respectively. C_1 and D_1 (C_2 and D_2) depict the initial (final) locations of the 5- and 1.667-km-resolution domains, respectively. Letter "H" denotes portion of the eastern Canadian high pressure system with an arrow highlighting its associated easterly flow.

changes at its later stages when it was advected into Sandy's core region and its surrounding areas.

Time series of the minimum central SLP P_{MIN} and the surface maximum wind V_{MAX}, given in Fig. 3a, shows that Sandy underwent multi-intensity changes during the study period of 0000 UTC 24 October–1800 UTC 29 October 2012. They could be divided into the following four distinct stages: (i) RI, (ii) weakening, (iii) steady V_{MAX} but with continued falls in P_{MIN}, and (iv) reintensification. During the RI stage of 0000 UTC 24 October–0600 UTC 25 October, V_{MAX} increased from 28 to 51 m s^{-1} (i.e., category-3 intensity) with a 24-h intensifying rate greater than the RI rate defined by Kaplan and DeMaria (2003), while P_{MIN} decreased from 990 to 954 hPa. Sandy weakened rapidly to category-1 intensity (i.e., 33 m s^{-1}) after making landfall at Cuba near 0600 UTC 25 October, and its weakening continued, albeit at a reduced rate, even after it moved across Cuba into a warm SST region. The value of V_{MAX} remained nearly constant—for example, varying between 30 and 35 m s^{-1}, so called the steady-V_{MAX} stage, during the 48-h period of 1800 UTC 26 October–1800 UTC 28 October. Of interest is that while V_{MAX} changed little in amplitude, P_{MIN} kept dropping by a total of 19 hPa in 48 h despite Sandy moving over a colder-SST region (cf. Figs. 1a and 3a). Thus, as one of the objectives of this study, we must address what process could account for such an unusual phenomenon—namely, continuous drops in P_{MIN} but with little changes in V_{MAX}. The storm reintensified during the period of 1800 UTC 28 October–1800 UTC 29 October, with V_{MAX} reaching to a secondary peak value of 43 m s^{-1} (i.e., category-2 intensity) just prior to landfall. To understand these unusual intensity changes of the storm, especially its associated structural and size changes, we have to invoke high-resolution simulations of the case, as described below.

3. Model description and verification

a. Model description

In this study, Hurricane Sandy is explicitly simulated using the two-way interactive, quadruply nested-grid (45, 15, 5, and 1.667 km) version 3.4.1 of the WRF Model with the finest grid size of 1.667 km (Skamarock et al. 2008). Horizontal (x, y) dimensions for the nested 45-, 15-, 5-, and 1.667-km domains are 250 × 170, 361 × 406, 475 × 475, and 709 × 709, respectively (Fig. 1b). The 5- and 1.667-km-resolution domains are storm-following nests, with the storm centered in them. In the vertical, 44 sigma levels are used with higher resolution at the bottom and upper levels. The model top is set at 30 hPa. All domains are initialized at 0000 UTC 24 October, which is just prior to the onset of RI, and integrated 138 h until 1800 UTC 29 October (i.e., shortly after Sandy reached its second intensity peak).

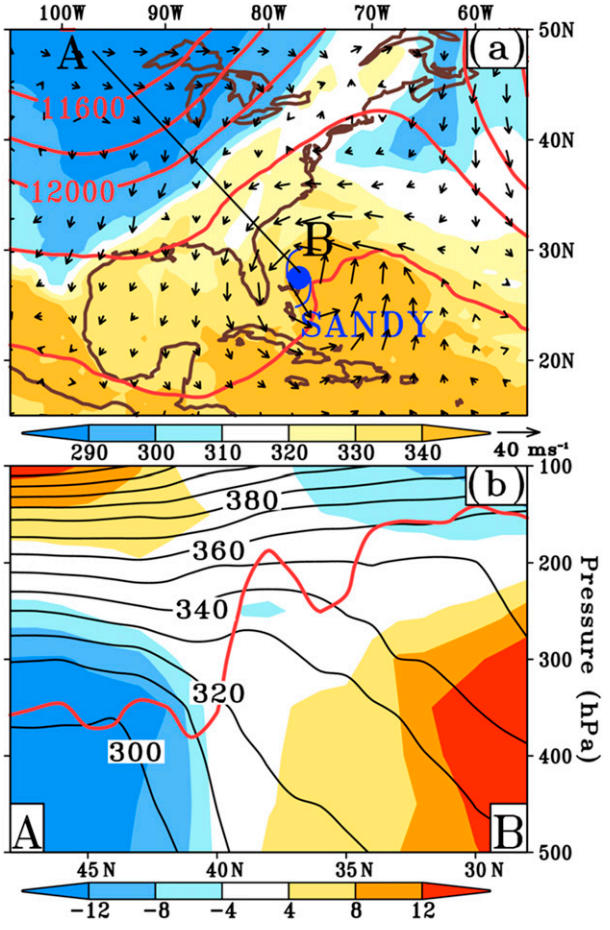

FIG. 2. (a) The NCEP final analysis of the equivalent potential temperature θ_e (shaded, K) and horizontal wind vectors at 900 hPa and the geopotential height (red contours at intervals of 200 m) at 200 hPa at 0000 UTC 27 Oct 2012. A hurricane symbol indicates the location of Sandy here and in the rest of figures. (b) Vertical cross section of potential temperature (black contours at 10-K intervals), the dynamic tropopause defined by a 2-PVU red line, and temperature deviations (shaded, °C) from the corresponding level-averaged value along line AB given in (a). All fields are ±110 km laterally averaged on the meridional direction.

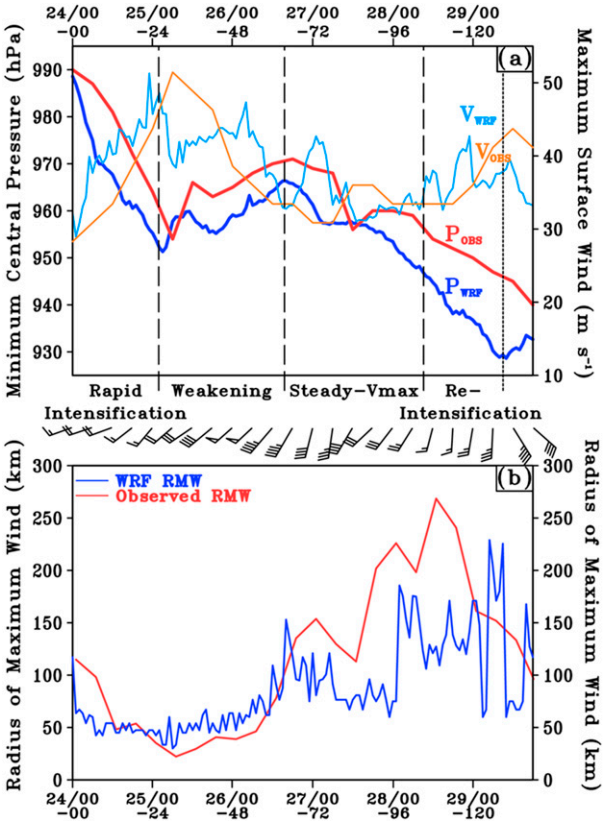

FIG. 3. (a) Time series of the simulated minimum central pressure P_{WRF} (thick blue) and maximum surface wind V_{WRF} (thin blue) and the corresponding best-track data (P_{MIN}: thick red; V_{MAX}: thin orange) during the period of 0000 UTC 24 Oct to 1800 UTC 29 Oct 2012. Note that V_{WRF} is obtained within a 300-km radius from Sandy's vortex center. Time series of wind barbs (full barb = 5 m s^{-1}), given at 6-h intervals, represent (1000 km × 1000 km) area-averaged vertical wind shear in the 200–850-hPa layer. Four distinct development stages are defined, based on the model simulation (see text) here and in the rest of figures. (b) Time series of the simulated (blue) and observed (red) RMW (km). Data from the WRF 15-km-resolution domain are used.

An advanced bogussing algorithm developed by Kwon and Cheong (2010) is applied. To follow their bogussing algorithm, the NCEP 1°-resolution final analysis is interpolated onto 0.175°-resolution data and then used to specify the model initial and outermost lateral boundary conditions. A bogus vortex is implanted into the interpolated NCEP final analysis at the model initial time, based on the NHC's best-track data (i.e., P_{MIN}, location, V_{MAX}, and 17 m s^{-1} wind radius). SSTs are specified from the 0.25°-resolution Advanced Very High Resolution Radiometer (AVHRR) SST data at the model initial time, and they remain constant during the 138-h simulation period. This high-resolution SST dataset appears to be important for obtaining realistic simulations because it resolves the narrow Gulf Stream (Fig. 1a).

The model physics schemes used include (i) the Kain–Fritsch cumulus parameterization scheme (Kain 2004) for the three outer domains, (ii) the WSM5 single-moment 5-class microphysics scheme (Hong et al. 2004; Hong and Lim 2006) for all the domains, (iii) the Yonsei University planetary boundary layer (PBL) parameterization with the Monin–Obukhov surface-layer scheme (Hong et al. 2006), (iv) a modified surface flux scheme for high surface winds (Donelan et al. 2004; Davis et al. 2008a), and (v) the Rapid Radiative Transfer Model (RRTM) scheme for longwave (Mlawer et al. 1997) and Dudhia (1989) shortwave radiation. The WSM5 scheme is used herein because it reproduces better the track and intensity, and especially rainband

structures than the WSM6 scheme during Sandy's reintensification stage.

b. Model verification

Before the model simulation can be used to analyze Sandy's meso-β-scale structures and evolution, it is necessary to verify it against all available observations. It is apparent from Fig. 1a that the WRF reproduces remarkably well the best track during the 138-h integration period, including Sandy's curved movements and relative position to the Gulf Stream. However, the simulated storm begins to move poleward notably faster than the observed after 24 h into the integration—that is, from 0000 UTC 25 October, herein referred to as 25/00-24. The simulated 5-day track error at 29/00-120 is 220 km, which is smaller than the official 5-day forecast error of 275 km (Blake et al. 2013). Because of the faster movement, the simulated storm begins its northwestward recurvature about 6 h earlier than the observed around 29/06-126. As a result, the simulated Sandy moves across the Gulf Stream and reaches its second peak intensity slightly earlier than the observed.

The time series of P_{MIN} and V_{MAX} between the best track and WRF simulation is compared in Fig. 3, showing that despite some differences in details due partly to different spatial and temporal resolutions between the WRF simulation and best track, the model reproduces reasonably well the above-mentioned four distinct stages: RI, weakening, steady V_{MAX}, and reintensification. Because of the slightly faster poleward movements, the simulated storm reaches its first peak intensity in P_{MIN} and V_{MAX} of 952 hPa and 49 m s^{-1}, respectively, around 25/02-26, which occurs just prior to landfall on Cuba, about 4 h earlier than the observations. Then, it decays to its weakest intensity of 966 hPa and 33 m s^{-1} around 26/16-64, and reintensifies to its second peak intensity of 929 hPa and 38 m s^{-1} shortly after passing across the Gulf Stream at 29/10-130 (cf. Figs. 1a and 3).

The model simulates on average the intensifying rate of about 34 hPa day^{-1} in P_{MIN} and more than 16 m s^{-1} day^{-1} in V_{MAX} during the RI stage (i.e., from 24/00-00 to 25/02-26) and the weakening rate of about 9 hPa day^{-1} in P_{MIN} and 10 m s^{-1} day^{-1} in V_{MAX} during the weakening stage (i.e., from 25/02-26 to 26/16-64), the fluctuating V_{MAX} around 35 m s^{-1} but the continued deepening rate of 11 hPa day^{-1} during the steady-V_{MAX} stage (i.e., from 26/16-64 to 28/10-106) and the intensifying rate of 17 hPa day^{-1} in P_{MIN} and about 3 m s^{-1} day^{-1} in V_{MAX} during the reintensification stage (i.e., from 28/10-106 to 29/10-130). The four stages coincide with the periods of moderate VWS (i.e., varying between 11 and 7 m s^{-1} in the 200–850-hPa layer), increasing VWS (i.e., from 7 to 26 m s^{-1}), intense VWS but with decreasing magnitudes at the later period (i.e., from 26 to 9 m s^{-1}), and increasing VWS once again (i.e., from 9 to 21 m s^{-1}), respectively (Fig. 3a). The two periods of increasing VWS correspond to Sandy approaching to a jet stream ahead of two upper-level troughs, respectively. It is encouraging that the model reproduces well the magnitude of $V_{MAX} \sim 35$ m s^{-1} and the observed mean deepening rate in P_{MIN} during the steady-V_{MAX} stage.

A comparison of the simulated RMW to that in the Hurricane Research Division Real-time Hurricane Wind Analysis System (H*Wind) data (Powell et al. 1998) also shows that the model captures the initial rapid contraction to 50 km and the subsequent near-constant RMW during RI and the later expansion of the RMW to about 150 km (Fig. 3b). The simulated RMW exhibits pronounced fluctuations (i.e., between 60 and 200 km) after 28/00-96 because of the development of another RMW associated with an intense spiral band in the outer regions, as will be shown in section 4a. The smaller RMW associated with the eyewall decreases from about 110 to 60 km during the reintensification stage, which is consistent with the contraction of Sandy's vortex in the H*wind data.

To show further the quality of the model simulation, Fig. 4 compares the simulated cloud structures to the observed outgoing longwave radiation (OLR) at cloud top. Sandy exhibits a typical mature TC's structures shortly after reaching its first peak intensity from both the simulation and satellite infrared image (IR) (cf. Figs. 4a and 4e), with a clear eye inside a full eyewall and two spiral rainbands (an inner one spiraling from the northwestern to southeastern quadrant and then to the southwestern quadrant and an outer rainband extending from the northwestern to northeastern quadrant). The weakening stage corresponds to reduced convective activity in the eyewall and scattered clouds in the inner and outer rainbands (Figs. 4b and 4f). The steady-V_{MAX} stage is characterized by an eyewall that is somewhat separated from an extensive, wide outflow channel associated with the outer rainband as it moves cyclonically to the western semicircle (cf. Figs. 4c and 4g). At the final stage, this outflow channel extends from the southern semicircle to eastern Canada with a much smaller-sized eyewall (Fig. 4h). As will be discussed in section 4a, rainbands "A," "B," and "C" are closely associated with warm frontogenesis. The WRF captures well these structures and their changes, especially the two separate spiral rainbands (i.e., B and C in Figs. 4d,h), except for inner-core cloud activity during the final two stages (cf. Figs. 4c,g and 4d,h).

Figure 5 shows a close-up of the simulated rainbands compared to microwave imageries during the last two

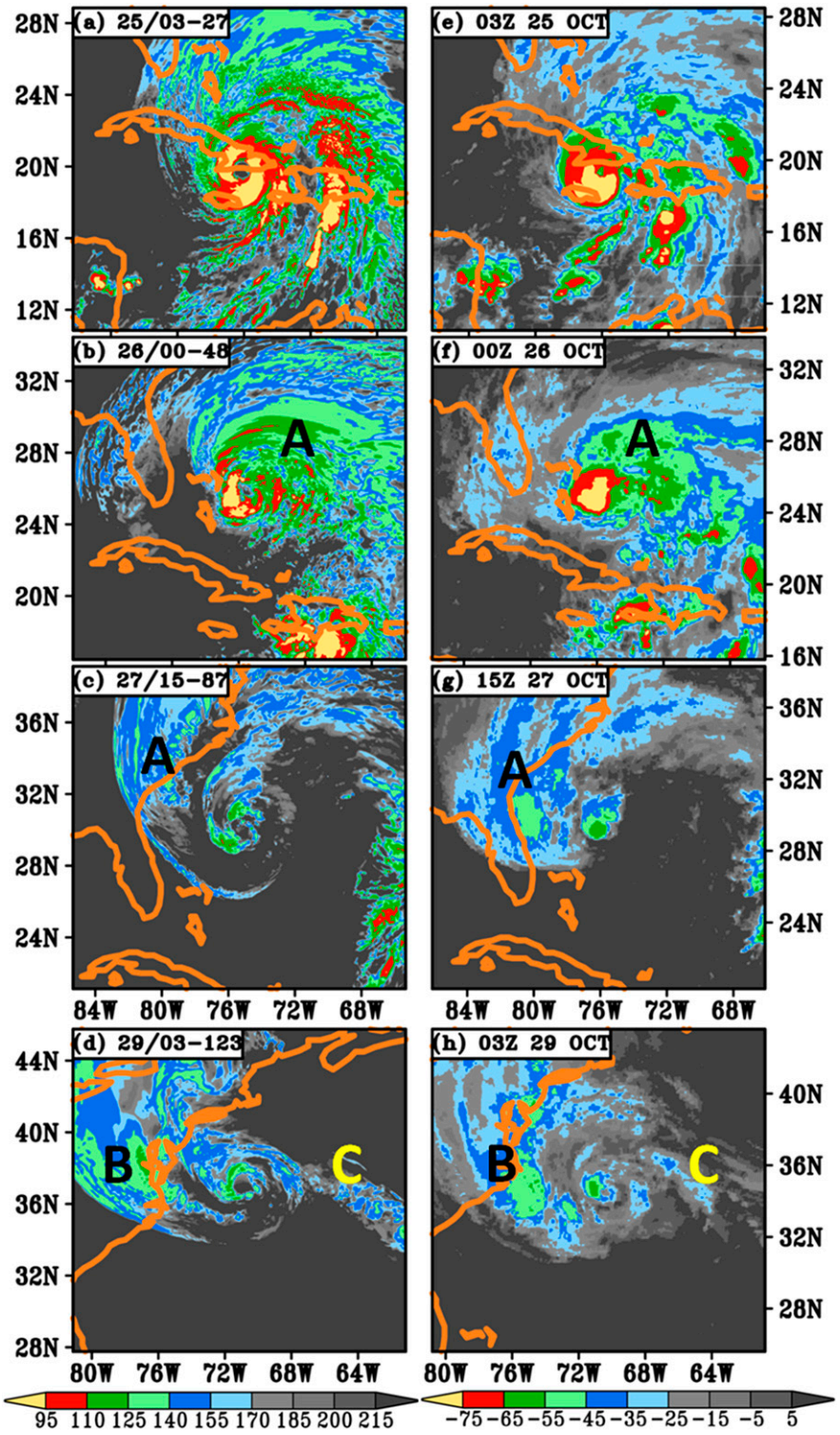

FIG. 4. (a)–(d) The simulated outgoing longwave radiation (OLR, shaded, W m^{-2}) from the 5-km-resolution domain at 25/03-27, 26/00-48, 27/15-87, and 29/03-123, respectively. (e)–(h) As in (a)–(d), respectively, but for the satellite IR images (brightness temperature, shaded, °C) at the given time from the Gridded Satellite (GridSat-B1) data archive of National Climatic Data Center of NOAA (http://www.ncdc.noaa.gov). Letters, A, B, and C indicate frontal rainbands corresponding to those shown in Figs. 5 and 6.

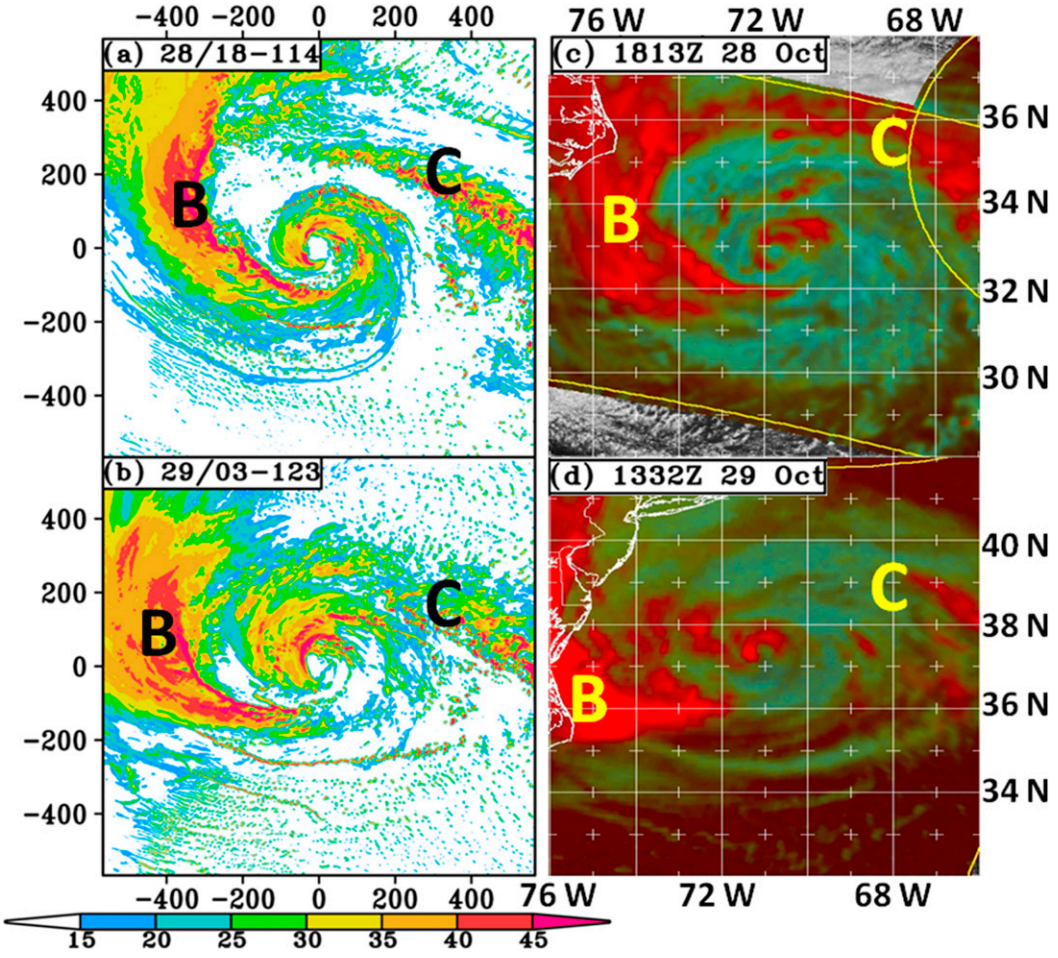

FIG. 5. (a),(b) The simulated composite radar reflectivity (shaded, dBZ) from the 1.667-km-resolution domain at 28/18-114 and 29/03-123, respectively. (c),(d) Microwave image of Sandy from the NRL web page (http://www.nrlmry.navy.mil/tc_pages/tc_home.html) at 1813 UTC 28 Oct and 1332 UTC 29 Oct, respectively. Areal sizes are similar between the simulation and observations. The model simulation at 29/03-123 is used to compare with the observation at 1332 UTC 29 Oct, because the simulated storm begins its reintensification earlier than the observed. Letters B and C indicate frontal rainbands corresponding to those shown in Figs. 4 and 6.

stages. Sandy had three distinct rainbands (Figs. 5c,d); one associated with the partial eyewall, a major spiral rainband B in the western semicircle, and another rainband C interacting with the cold air mass to the north. All the above rainbands are reasonably captured by the simulation, including their locations, general distribution, and sizes, which will be discussed in more detail in section 4a.

Based on the above verifications, we may state that the WRF simulates reasonably well the life cycle of Hurricane Sandy (2012) in terms of track and intensity changes, even though later stages begin somewhat earlier than the observations. The WRF also reproduces well the structural and size evolution of the storm, including the RMW and cloud coverage. Thus, the model simulation could be used in the next to address the objectives of the present study and examine some nonobservable features of the storm. Because of the timing errors with the track, the four distinct development stages will be based on the model-simulated wind intensity for the sake of subsequent discussions.

4. Multiple intensity, size, and structural changes

In this section, we present the evolution of Sandy's intensity, size, and structural changes and then examine the relative contributions of low- and upper-level processes to these changes using the model-simulation data.

a. Structural evolution

Figure 6 shows the horizontal structural evolution of Sandy during its four different stages. At the first peak

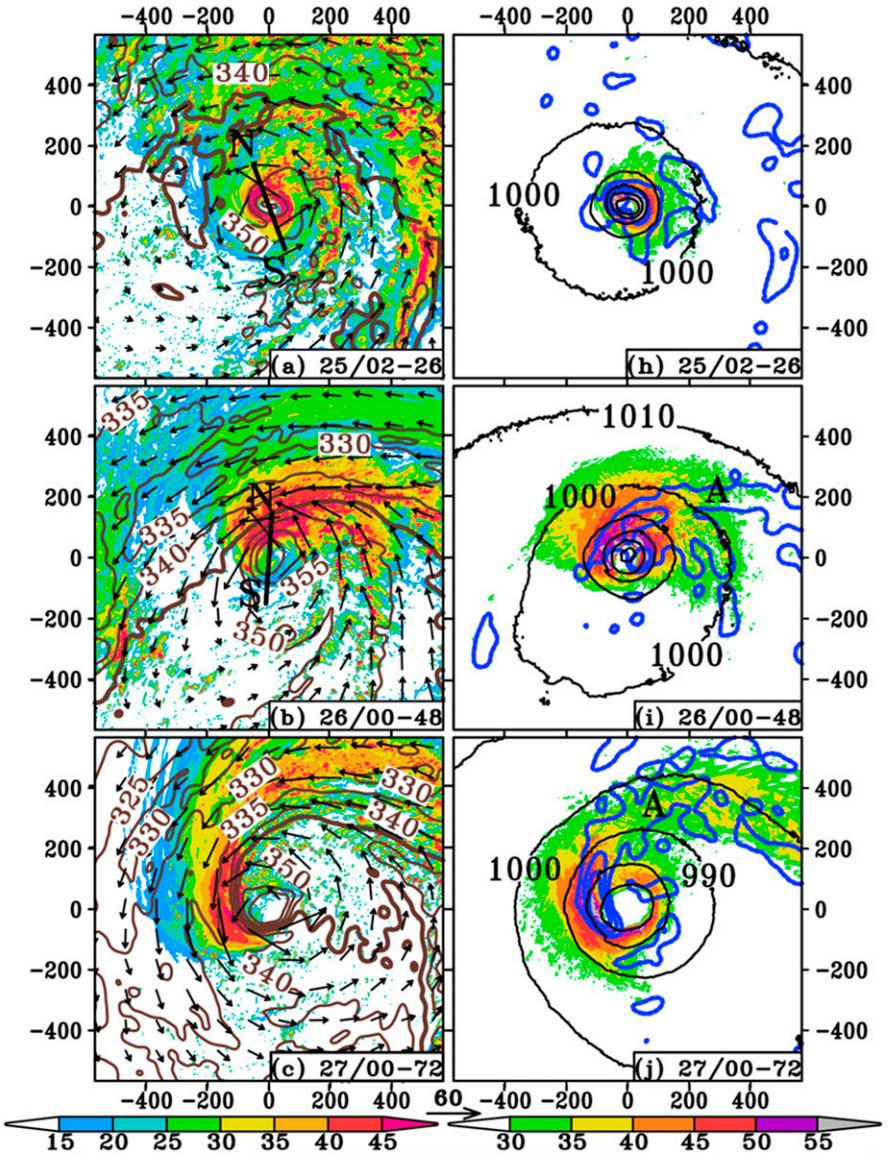

FIG. 6. (a)–(g) Horizontal distribution of composite radar reflectivity (shaded, dBZ), equivalent potential temperature θ_e (contoured at 5-K intervals with θ_e = 310 and 345 K highlighted in brown), and horizontal wind vectors at z = 1 km from the WRF 1.667-km-resolution (1134 km × 1134 km) subdomain, valid at 25/02-26, 26/00-48, 27/00-72, 28/00-96, 28/18-114, 29/03-123, and 29/09-129, respectively. Line NS denotes the locations of vertical cross sections shown in Fig. 13. (h)–(n) As in (a)–(g), respectively, but for horizontal distribution of SLP (black contours at 10-hPa intervals), horizontal wind speeds (shaded, m s^{-1}), and two-dimensional scalar frontogenesis function [blue contours at −4, −20, and −40 K (100 km)$^{-1}$ h^{-1}, with negative values implying frontogenesis] at z = 1 km. Letters, A, B, C, D, and E, shown in (i)–(n), denote various frontal rainbands (see text). Horizontal and vertical axes indicate the distance (km) from Sandy's vortex center.

intensity near 25/02-26, we see typical cloud structures (Figs. 4a and 6a) and wind–pressure fields (Fig. 6h) associated with a mature TC: a well-defined eye, and a relatively compact and symmetric eyewall with an RMW of about 50 km, several spiral rainbands distributed mostly in the northeastern outer semicircle, and dense (very coarse) isobars in the inner-core (outer) regions. In addition, Sandy is surrounded by higher (lower)-than-345-K-θ_e air of tropical (polar) origin in the southern (northern) environment. As VWS increases and Sandy weakens, the more symmetric rainfall distribution in the eyewall evolves gradually to a

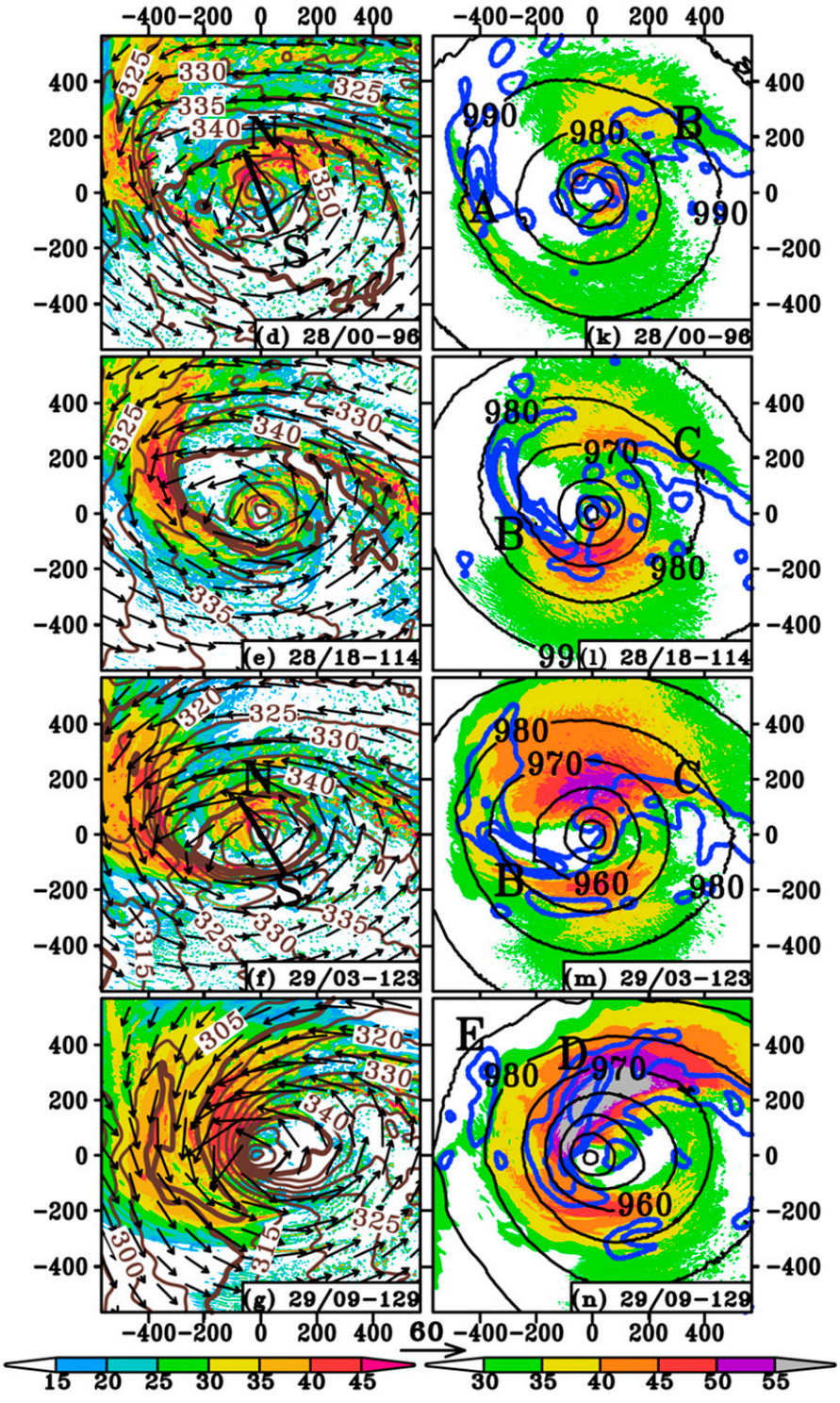

FIG. 6. (*Continued*)

wavenumber-1 structure, with intense precipitation occurring on the downshear-left side—that is, in the northwestern quadrant (cf. Figs. 4a,b and 6a,b). Similarly, the TC circulation becomes elliptically shaped, with its low-SLP center close to more active convection to the northwest. Meanwhile, Sandy's northward movement over cooler water toward the northern baroclinic zone associated with the eastern Canadian high

tends to decrease θ_e in the PBL and increase meridional θ_e gradients, as indicated by the approaching lower-than-330-K-θ_e air in the north (Fig. 6b). In particular, Sandy's south- to southeasterly high-θ_e current converges with this easterly lower-θ_e current in the northeastern quadrant (e.g., along the θ_e = 345-K contour), leading to the formation of a warm-frontogenetic zone (labeled as A in Fig. 6i) with increased θ_e gradients, along which a robust spiral rainband is developed (Figs. 6b,i). This type of frontogenesis, though shown herein by high-θ_e gradients but defined by a scalar frontogenesis function (blue in Figs. 6h–n) associated with divergence and horizontal deformation on horizontal θ gradients [see Eq. (2.6a) in Keyser et al. (1988)], is a typical feature of ET (Klein et al. 2000; Jones et al. 2003; Colle 2003). Note that warm frontogenesis discussed herein does not include the eyewall although it shows significant frontogenesis processes. Clearly, deep convection associated with frontogenesis would enhance the mass and moisture convergence, facilitating the generation of wind streaks and SLP falls through cyclonically inward advection of the absolute angular momentum (AAM), as discussed by Yau et al. (2004). It would also augment the frontogenetic forcing, assisting further convective organization. This interactive process can be seen beginning from Sandy's weakening to steady-V_{MAX} stages (Figs. 6i,j), as a swirling jet exceeding 30 m s^{-1} starts to develop along the outer frontogenetic zone.

Because of the asymmetric locations of the eyewall convection relative to the low SLP center, Sandy's movement exhibits trochoidal oscillations as shown by Neuman and Boyd (1962), and Liu et al. (1999), with the associated vortex core being advected within a larger-scale elliptically shaped circulation (Figs. 6b,c). By 27/00-72, we see a comma-shaped swirling jet varying from over 55 m s^{-1} in the eyewall to 35 m s^{-1} at radius R = 500 km, which corresponds to the distribution of the eyewall convection and spiral frontal rainband A (Figs. 6c,j). At 28/00-96, the cyclonic advection of the vortex core within the elliptically shaped circulation, plus easterly flows outside 200-km radius associated with the eastern Canadian high (cf. Figs. 6d and 1b), almost decouples the eyewall convection from the frontal rainband A, as the latter is fast advected to the northwest (cf. Figs. 6c and 6d). Of interest is the development of another frontogenetic zone (labeled B in Fig. 6k) with a spiral rainband in the northeastern quadrant, which occurs again as Sandy's southeasterly flow converges with the easterly flow (Figs. 6d,k). For the same reason, a third frontogenetic zone/rainband, labeled C in Fig. 6l, develops in Sandy's northeastern quadrant by 28/18-114. In contrast, little cloud activity occurs in the southeastern semicircle where upward motion is suppressed in the inner-core region by intense southwesterly to southerly VWS and in the outer region owing to the presence of diffluence (i.e., frontolysis). As a result, Sandy exhibits three convective bands: one in the partial eyewall, and the others along the two warm fronts, with the corresponding local wind streaks (Figs. 6d,k).

Note the weakening of wind streaks along rainband A at 28/00-96 and portion of rainband B at later times, even in the presence of organized deep convection and strong frontogenetic forcing. This can be understood as a result of the radially outward advection of AAM by the intense easterly flow (Figs. 6d,k and 6e,l). On the other hand, wind streaks remain in the outer northeastern quadrant where the radially inward advection of AAM occurs along the frontal rainband. It is the amplitude changes of the wind streaks that account for the fluctuation of the RMW in Fig. 3b. This also explains that the frontal rainbands contribute more to the increased wind intensity in the outer regions, whereas the local V_{MAX} is more determined by the eyewall convection during the weakening and steady-V_{MAX} stages.

Sandy's reintensification stage is dominated by (i) a well-developed wavenumber-1 precipitation pattern on the downshear left, as southerly VWS increases to about 20 m s^{-1} (cf. Figs. 6f,g and 3a); (ii) the generation of a wind streak associated with a partial eyewall in the northern semicircle (Figs. 6f,m); (iii) merging of the final two frontogenetic zones and the partial eyewall into a spiral intensifying frontogenetic zone/rainband "D" extending from the southwestern partial eyewall to outer northeastern quadrant (Figs. 6m,n), as the frontal rainband A diminishes shortly after 28/00-96; and (iv) an inward-spiraling jet of greater than 55 m s^{-1} along the merged frontogenetic zone and eyewall (Fig. 6n). Note that the vortex contraction, as shown in Fig. 3b, may be considered as the cyclonic inward contraction of the jet core, representing Sandy's intensity, along the intensifying frontogenetic zone, where the cyclonic inward advection of AAM is further enhanced. Note also the substantial reduction of the higher than θ_e = 345-K coverage after 28/00-96, due partly to Sandy's movement over cooler water and partly to the impact of moist downdrafts through lower-θ_e layers above, indicating the importance of baroclinic processes in determining Sandy's reintensification. It should be mentioned that because of their model initialized at 28/00, Galarneau et al. (2013) could only simulate reasonably well the development of a major warm-frontal rainband extending from Sandy's northwestern to northeastern quadrants at 18 h into the integration (see their Figs. 8–10), which is similar to that of rainband B shown in Figs. 5 and 6e,l herein. However, they attributed its

development to surface heat fluxes associated with the Gulf Stream.

Apparently, it is (i) convectively enhanced (warm) frontogenesis resulting from interaction of the high-θ_e southeasterly flow with the low-θ_e easterly flow (i.e., moist frontogenesis) within Sandy's internal circulation that leads to the generation and continued size expansion of the tropical storm–force wind and (ii) the merging of two frontogenetic zones and the partial eyewall, and the subsequent cyclonic inward progression of the jet core along the enhanced frontal rainband, that account mostly for Sandy's reintensification. This implies that the frontogenetically enhanced rotational flows in the outer regions during the weakening and steady-V_{MAX} stages tend to precondition the AAM therein and then contribute to Sandy's reintensification through the cyclonic inward advection, as mentioned above. On the other hand, the large-scale cold front, traced by $\theta_e = 310$ K at $z = 1$ km (Figs. 2a and 1b), just enters the western boundary of the analysis domain at 29/03-123 (Fig. 6f), and it generates an elongated narrow rainband along a frontogenetic zone, labeled as "E" in Fig. 6n, near $R = 400$ km when converging with the eastern Canadian air of the same coldness (as shown by a cyclonically oriented θ_e = 310-K tongue) at 29/09-129 (Fig. 6g). There is no doubt that this cold front could influence the storm's intensity and structures after its landfall (Galarneau et al. 2013). Note that lower-than-310-K-θ_e air of polar origin has not encircled the warm-cored storm at 29/09-129, unlike the warm seclusion shown by Galarneau et al. (2013), and it should remain so as long as the warm frontogenesis continues.

Figures 6i–m also show continuous meso-α-scale SLP falls after 26/00-48, including P_{MIN} (Fig. 3), while V_{MAX} remains nearly a steady state. For example, the radius of the 980-hPa isobar expands from 80 km at 26/00-48 to 200 km at 28/00-96 and over 400 km at 29/03-123. The isobar keeps expanding eastward subsequently, while its western semicircle shrinks in radius in the presence of deep convection, thereby increasing local radial pressure gradient force (PGF_R) and rotational winds (cf. Figs. 6g,n). One may ask: Why could the lower SLP coverage and the associated cyclonic circulation expand dramatically while V_{MAX} experiences little changes in amplitude? In this regard, Wang (2009) shows, using an axisymmetric TC-like model, that an outer spiral rainband tends to cause SLP falls on its inward side where the inertial stability is relatively high, increasing the coverage of SLP falls. Similar results have been shown by Hill and Lackmann (2009) in the context of convectively generated PV along spiral rainbands. This indicates that diabatic heating in the outer region would likely reduce PGF_R, thereby decreasing V_{MAX}. However, unlike in Wang's experiment, Sandy has highly asymmetric spiral rainband structures, and pronounced SLP falls occur on both inward and outward sides, especially in the outer southeastern quadrant where little convective activity takes place. Thus, diabatic heating along the outer spiral rainband cannot explain the rapid expansion of the SLP falling area. As will be shown in the next subsection, the meso-α-scale SLP falls are associated mainly with the advection of warmer air in the lower stratosphere from the northwest. More pronounced SLP falls occur in both the inner-core and outer regions after entering the reintensifying stage, which are qualitatively consistent with the contraction of Sandy's vortex and increasing rotational flows in both the eyewall and spiral rainband. Only near the western boundary of the analysis domain at 29/09-129, SLP exhibits a sign of slow rising as a result of the approaching cold front (cf. Figs. 6m and 6n).

The time series of azimuthally averaged fields, given in Fig. 7a, summarizes Sandy's intensity and size changes during the four different stages. One can see intensifying swirling winds accompanied by rapid central SLP falls with time, with strong radial SLP gradients in the inner-core region, and a rapidly reducing RMW (in the first 6–12 h) followed by a near-constant RMW during the RI stage; slowly weakening flows and SLP gradients with an increasing RMW, and slow central SLP filling during the weakening stage; slowly evolving swirling winds in spite of significant contraction, and the later formation of spiral rainbands, but pronounced central SLP falls during the steady-V_{MAX} stage; and a decreasing RMW, increasing winds and SLP falls during the final stage. Of significance is the expansion of intense swirling flows (e.g., greater than 25 m s^{-1}) and storm-scale SLP drops (e.g., encompassed by the 990-hPa isobar) from $R = 120$ km at 25/12-36 to $R = 500$ km at the end of the steady-V_{MAX} stage, and even larger at the later stages, making Sandy a record-breaking storm size. Note again that the SLP field keeps dropping in both the outer- and inner-core regions during the steady-V_{MAX} stage, as also shown in Figs. 6i–l, and at a similar rate, as indicated by near-linear distribution of isobars out to $R = 500$ km.

An analysis of the azimuthally averaged AAM and radial flows in Fig. 7b indicates two pronounced radial flow regions: one within $R = 200$–300 km during the early two stages and the other in $R = 80$–500 km at the final stage, with a broad range of weaker inflows during the steady-V_{MAX} stage. The above-mentioned storm size growth results from continuous inward advection of AAM by meso-α-scale convergence associated with a broader range of SLP falls, except for the core region where little radial inflows and AAM advection are present. A comparison of Figs. 7b and 7a indicates that

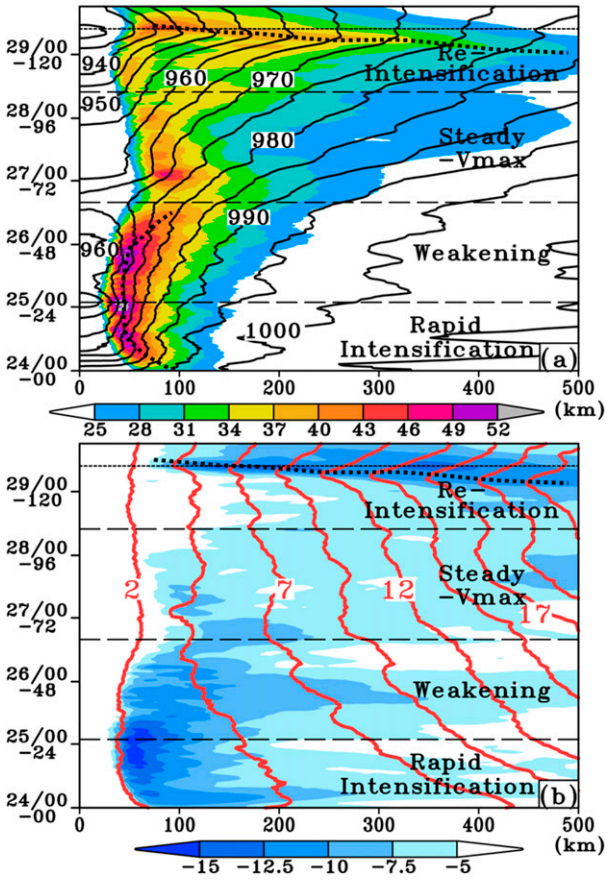

FIG. 7. Time–radius cross section of the azimuthally averaged fields: (a) tangential wind speeds (shaded, m s^{-1}) at $z = 0.5$ km and SLP (black contours at 5-hPa intervals) and (b) radial wind speeds (shaded, m s^{-1}) and AAM (red contours at intervals of 2.5×10^6 m^2 s^{-1}) at $z = 0.5$ km from the 138-h simulation of the WRF 1.667-km-resolution domain. Dotted lines in (a) and (b) denote the RMW and the ridge axis of AAM, respectively (see text).

the azimuthally averaged peak rotational wind in the PBL increases rapidly during the first 12-h RI stage because of the significant inward AAM advection and RMW contraction, maintains its strong intensity with a near-constant RMW until 26/00-48, and decreases later owing to the expansion of the RMW associated with the weakening eyewall convection but enhanced spiral rainband. The steady-V_{MAX} stage is characterized with much weaker (significant) inward AAM advection within (outside) $R = 150$ km. While the outer frontal rainband enhances cyclonic winds in the outer region via the inward AAM advection, the widespread SLP falls tend to suppress increases in PGF$_R$, thereby damping the inward AAM advection to the core region. This appears to explain why the rotational speed of Sandy changes little during the steady-V_{MAX} stage, in addition to the weakening of wind streaks along rainband A (Fig. 6k). As a result, Sandy exhibits a weak but broad cyclonic circulation structure during this stage (Fig. 7a). On the other hand, we see increasing PGF$_R$ and radial inflows at the reintensification stage, allowing for more significant inward advection of AAM and spinup of tangential winds starting from the outer regions inward—namely, from $R = 500$ km at 29/00-120 to $R = 100$ km at 29/10-130 [see dotted lines denoting the ridge (trough) axes of AAM and V_{MAX} (SLP) in Figs. 7a and 7b].

b. *Relationship between SLP falls and tropospheric–stratospheric warming*

Because SLP falls are hydrostatically associated with temperature changes in vertical columns, the area-averaged temperature changes [i.e., $\Delta T(z, t)$] from the initial time $T(z, t = 0\,\text{h})$ are given in Fig. 8, showing two distinct layers of warming tendencies during the final two stages: one in the (low to mid-troposphere) $z = 2$–7 km layer of 2°–8°C and the other in the layers above $z = 12$ km of up to 12°C, with little or negative warming tendencies in the intermediate layers. Zhang and Chen (2012) have demonstrated the more efficient roles of the upper-level warming than a lower-level one in reducing P_{MIN}. Figure 8 shows increasing warmth in both the lower and upper troposphere during the RI stage and more intense lower-tropospheric warming tendencies (denoted as "TW") but decreasing upper-level warming tendencies during the weakening stage. The more important roles of the upper-level warming can be more clearly seen from the subsequent steady-V_{MAX} stage, during which period the continuous P_{MIN} falls coincide well with increased warming tendencies in amplitude and depth in the lower stratosphere (denoted as "SW"), while the lower-tropospheric warming tendencies decrease. Note that the tropopause height becomes significantly lower after 26/16-64 as the storm moves to higher latitudes (cf. Figs. 8 and 2b). Rapid falls in P_{MIN} during the reintensification stage is consistent with increasing warming tendencies in both the lower stratosphere and troposphere. However, none of the previous studies of Sandy [e.g., by Galarneau et al. (2013) and Magnusson et al. (2014)] mentioned the presence of SW and its roles in determining the SLP (and P_{MIN}) changes. Thus, we have quantified the relative contributions of TW and SW to changes in P_{MIN}, following Zhang and Zhu (2012), and Cecelski and Zhang (2013), and found that TW accounts for 4–6-hPa fluctuations and falls in P_{MIN} during the steady-V_{MAX} and reintensification stage, respectively (not shown).

Figure 9 shows the height–radius (z–r) maps of warming [i.e., $\Delta T(r, z)$], and tangential winds, superimposed with in-plane flow vectors during the four

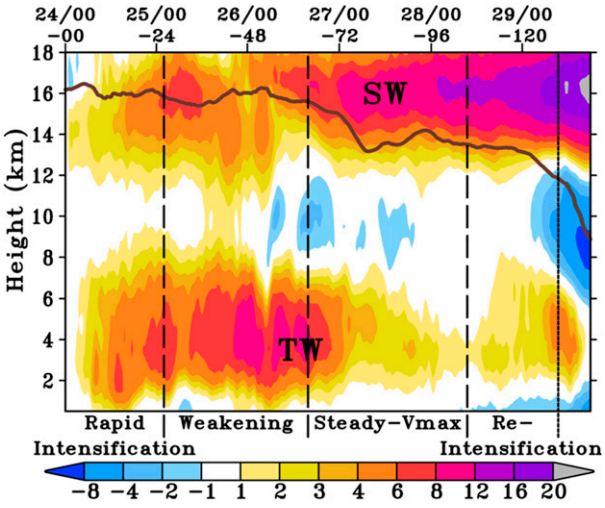

FIG. 8. Time–height cross section of temperature deviations $\Delta T(z, t)$ (shaded, °C), superimposed with the dynamical tropopause (brown) defined as the 500 km × 500 km area-averaged 2-PVU surface, taken at the storm center from the 138-h simulation, where $\Delta T(z, t)$ is defined as the (10 km × 10 km) area-averaged temperature $T(z, t)$ changes with respect to the same area-averaged temperature $T(z, t = 0\,\text{h})$ at the model initial time. Symbols "SW" and "TW" denote stratospheric and tropospheric warm deviations, respectively. Data from the WRF 1.667-km-resolution domain are used.

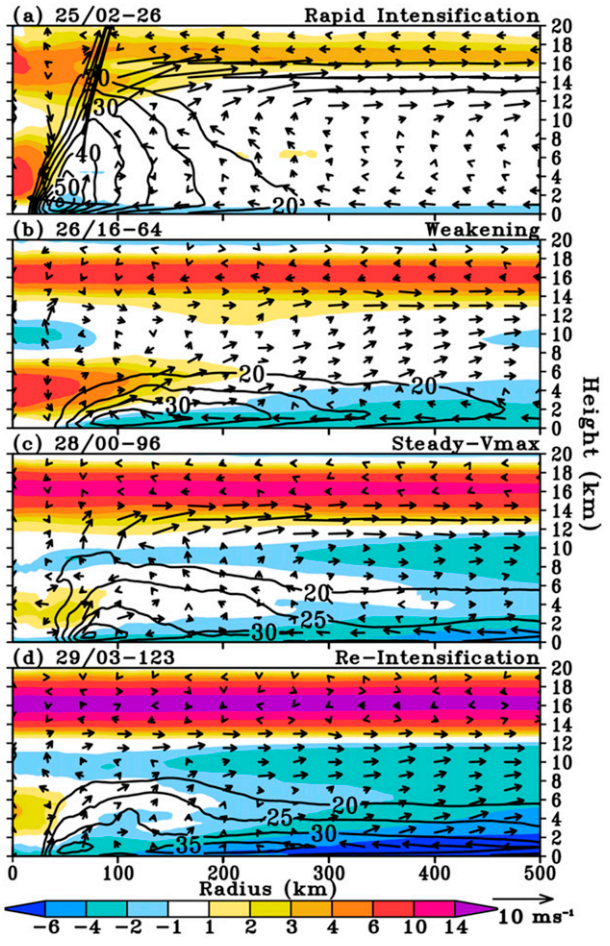

FIG. 9. Radial–height cross section of the azimuthally averaged temperature deviations $\Delta T(r, z, t)$ (shaded, °C), and tangential wind speed (contoured at 5 m s^{-1} intervals above 20 m s^{-1}), superimposed with in-plane flow vectors (with vertical velocity multiplied by 10) at (a) 25/02-26, (b) 26/16-64, (c) 28/00-96, and (d) 29/03-123 from the WRF 1.667-km-resolution domain. We define $\Delta T(r, z, t)$ as temperature changes with respect to $T(r, z, t = 0\,\text{h})$, which is the azimuthally averaged temperature at the model initial time. Horizontal axis indicates the distance (km) from Sandy's vortex center.

different stages. We see the development of an intense axisymmetric vortex with a peak intensity of more than 55 m s^{-1} at the end of the RI stage (i.e., 25/02-26) and then its peak intensity decreases to 35 m s^{-1} at 26/16-64, but reintensifies at 29/03-123 as the 35 m s^{-1} wind area expands significantly. Corresponding to the decreasing intensity is the general weakening of TW, except at 29/03-123. Of importance is the continuous increase in amplitude (i.e., from 3° to over 15°C) and depth (i.e., from 2.5 to 5 km) of SW near the tropopause or in the lower stratosphere, accompanied by the outward expansion of intense rotational flows. That is, the 30 m s^{-1} isotach coverage increases from R = 130 km at 25/02-26 to R = 270 km at 28/00-96 and over R = 500 km at 29/03-123. Of further importance is that unlike in the studies of Chen and Zhang (2013), this SW occurs above the upper-outflow layer even during the earlier stages when the upper outflows are intense (Figs. 9a,b). This implies that the overspread of the SW air is not related to Sandy's upper-level outflows. This is particularly true during the later stages when Sandy's rotation is shallow with little organized upper-level outflows (i.e., above z = 12 km; see Figs. 9c,d). Moreover, the SW air is not just distributed in the core region, unlike the presence of a typical TW core in the eye, but spread from the west to east through the core region, as will be further seen in the next subsection.

Figure 9 also shows indirectly the intrusion of cold air from higher latitudes, which is consistent with that shown in Figs. 6a–f. The cold intrusion into the proximity of the storm occurs first in the lowest 4-km layer after entering the weakening stage (cf. Figs. 9b and 6b). This shallow, PBL-based cold air mass originates from the eastern Canadian high (Fig. 1b), and it tends to wrap around the warm-core storm except in the northeastern quadrant where frontal rainbands develop frequently (Figs. 9c,d and 6d–g). Despite the deep-layer cold intrusion, Sandy still keeps its TC-like characteristics with a distinct midlevel warm core, even at the end of the 138-h simulation, albeit with decreased depth (and pronounced frontogenesis). Nevertheless, the cold-air

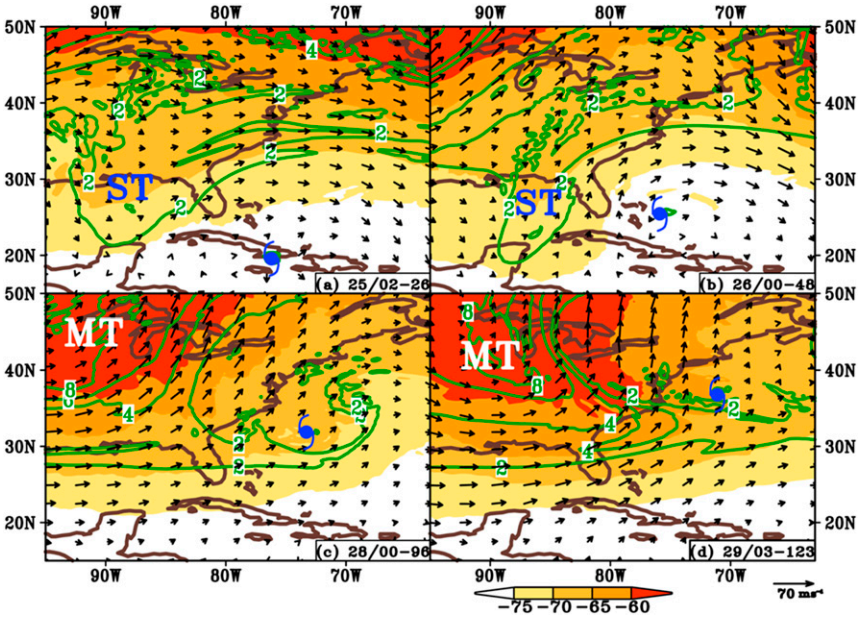

FIG. 10. Horizontal distribution of potential vorticity (contoured at 2, 4, 6, and 8 PVU) at $z = 12$ km (near 200-hPa level) and temperature (shaded, °C) and horizontal wind vectors at $z = 16$ km at (a) 25/02-26, (b) 26/00-48, (c) 28/00-96, and (d) 29/03-123 from the WRF 15-km-resolution domain. Symbols "ST" and "MT" indicate a subtropical short-wave trough and a midlatitude long-wave trough, respectively.

intrusion appears to help maintain radial thermal gradients, thereby sustaining Sandy's cyclonic circulation at hurricane intensity. This will be further discussed in the next subsection.

c. *Origin of the lower-stratospheric warmth and its influences*

After seeing the important contributions of the lower-stratospheric warming to P_{MIN} falls, it is desirable to examine its origin and the evolution of tropopause height during Sandy's poleward movement. Figure 10 presents the evolution of PV at $z = 12$ km and temperature and horizontal wind vectors at $z = 16$ km where the lower-stratospheric warming is peaked (Fig. 9). The lower stratosphere exhibits clearly a reversed temperature gradient from that in the troposphere (i.e., with warmer air poleward), as has also been shown in Fig. 2b. Sandy is located ahead of a weak subtropical trough (ST in Figs. 10a,b) at the early stages and then an intense midlatitude trough (MT in Figs. 10c,d). The tropopause, as defined by 2 PVU, is relatively lower at higher latitudes, especially undulating in the two troughs regions. As the ST dips southward at 26/00-48 (Fig. 10b), its associated lower-stratospheric warm air begins to interfere with Sandy's upper-anticyclonic outflow from the west. By 28/00-96, the core region has been warmed about 5°C (Fig. 10c). Note that the 2-PVU air wraps around the storm, implying that the ST with lower-tropopause heights has merged into Sandy's core region. Given the development of a shallow secondary circulation and weak intensity at this stage (Figs. 3a and 9c), the overspread of this warm air is clearly associated with the larger-scale circulation, rather than Sandy's upper-level outflows. This is more evident during Sandy's reintensification stage when the MT becomes northwest–southeast-oriented across the storm, with little evidence of convectively generated anticyclonic outflows (Fig. 10d). By this time, Sandy's lower-stratospheric environment has been warmed more than 10°C, including the core region (cf. Figs. 10b,d). Clearly, this could hydrostatically induce a large area of pressure falls in the deep tropospheric layers. Note that, owing to its faster propagation, the MT's influences on Sandy's inner-core circulation occur earlier than its corresponding surface cold front.

Figure 11 shows more clearly the vertical structure of tropopause undulation associated with the MT and its possible influences on Sandy's circulations. A 360-K isentropic surface analysis at 29/09-129 shows its rapid descent toward the bottom of the MT, forming a "warm pocket" in the southeastern quadrant of the storm (Fig. 11a). Figure 11b shows a sharp drop in tropopause height (down to 5.5 km) along the MT's cyclonic flow, which is more than 6 km lower than that in Sandy's immediate environment to the east. Associated with the lower-tropopause height are the gentle descent of

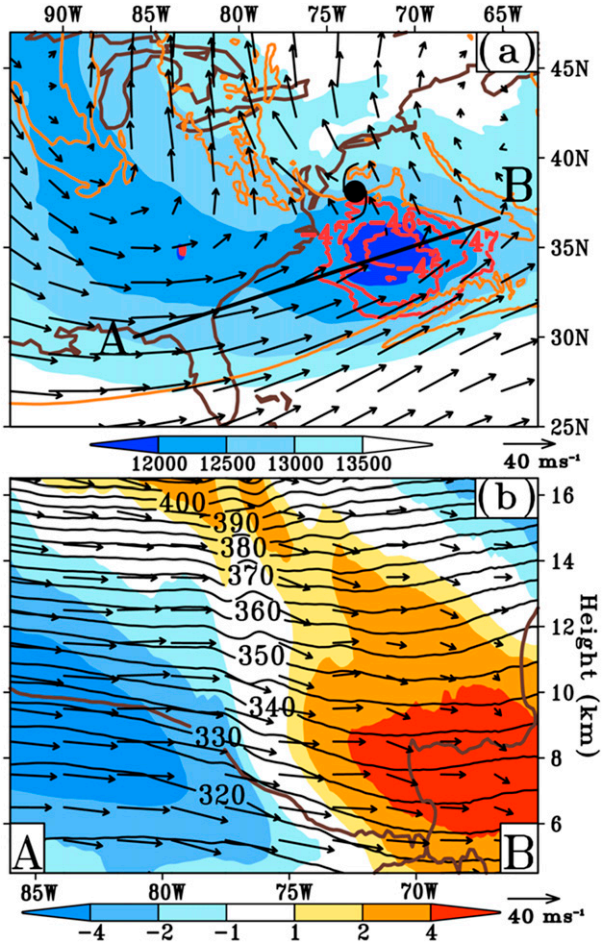

FIG. 11. (a) Horizontal distribution of the 360-K isentropic surface height (shaded, m) and wind vectors, 12-km potential vorticity (orange contours at 2 and 8 PVU), and temperature (red contours at −47°, −46°, and −45°C) at 29/09-129. (b) Vertical cross section of potential temperature (black contours at 5-K intervals), the dynamic tropopause defined by the 2-PVU line (brown), in-plane flow vectors (with vertical velocity multiplied by 100), and temperature deviations (shaded, °C) along line AB given in (a). Data from the WRF 15-km-resolution domain are used.

stratospheric air and downward sloping of isentropic surfaces and the formation of a deep-layer (5.5–14 km) warm anomaly.

The above scenarios are similar to the work of Hirschberg and Fritsch (1991a,b), who studied the relationship between tropopause undulations and extratropical cyclogenesis downstream. They found that the tropopause height in the upper-level trough region is lower than its environment because of descending warm stratospheric air. They claimed that the upper-level warm advection from this upstream region induces surface SLP falls leading to surface cyclogenesis. Similarly, through the use of 54.96-GHz microwave images, Velden (1992) noted the important roles of a warm anomaly at the tropopause in the extratropical surface cyclogenesis. Although some previous studies have shown the interaction between tropopause undulation and TCs (e.g., Bosart and Lackmann 1995; Atallah and Bosart 2003), few have examined the relative influences of the associated stratospheric warmth versus diabatic heating on TC intensity and structures.

It is obvious that the advection of the lower-stratospheric warm air across the storm must also affect Sandy's spatial distribution of SLP falls. To this end, the same methodology as that used by Zhang and Zhu (2012) and Cecelski and Zhang (2013) is adopted to estimate the relative influences of lower-stratospheric (SW_H) and tropospheric (TW_H) warming on the horizontal distribution of SLP falls. As a first step, the model-simulated SLP distributions, like those shown in Figs. 6h–n, are reproduced by integrating the hydrostatic equation from the model top to sea level with the total temperature field; that is, $T(x, y, z, t) = T(x, y, z, t = 64\,\text{h}) + \Delta T(x, y, z, t)$, where $\Delta T(x, y, z, t)$ is the temperature difference field between time t and 26/16-64. Then, $\Delta T(x, y, z, t)$ in the layers below (TW_H) and above (SW_H) $z = 12$ km is used, together with $T(x,y,z, t = 64\,\text{h})$, to integrate the hydrostatic equation, respectively. The hydrostatically calculated results are given in Fig. 12, showing widespread SLP falls of large amplitudes (e.g., up to 15–36 hPa from 28/00-96 to 29/09-129, purple contours) relative to 26/16-64 over the analysis domain. In the absence of TW_H, SW_H produces much greater SLP falls than the total (e.g., up to 21–60 hPa from 28/00-96 to 29/09-129), with the amplitudes decreasing cyclonically from the northwestern to southeastern corner (Figs. 12d–f). The general patterns of the SLP falls and mass-weighted SW_H at 29/09-129 correspond well to the cyclonic warm advection associated with the upper-level trough (cf. Figs. 12f and 11a). From PV perspective, we may attribute the large pressure falls to the arrival of upper-tropospheric cyclonic PV. Clearly, it is the eastward and then cyclonic progression of the SW_H air that results in the widespread SLP falls.

In contrast, the SLP falls induced by TW_H during the steady-V_{MAX} stage are small in both amplitude and coverage (Fig. 12a). Because the mass-weighted TW_H at 28/00-96 relative to 26/16-64 occurs mainly behind the western frontal rainband, it induces little SLP falls in the core region, but 6–9 hPa drops over an elliptic-shaped area corresponding to the TW_H distribution in the western semicircle (cf. Figs. 12a and 6d). Subsequently, the outer regions experience rapid SLP rises as they are gradually filled by colder air from the eastern Canadian high, except in the northeastern quadrant that is influenced by warm frontogenesis (cf. Figs. 12c and 6n). For instance, the mass-weighted TW_H in the warm southern

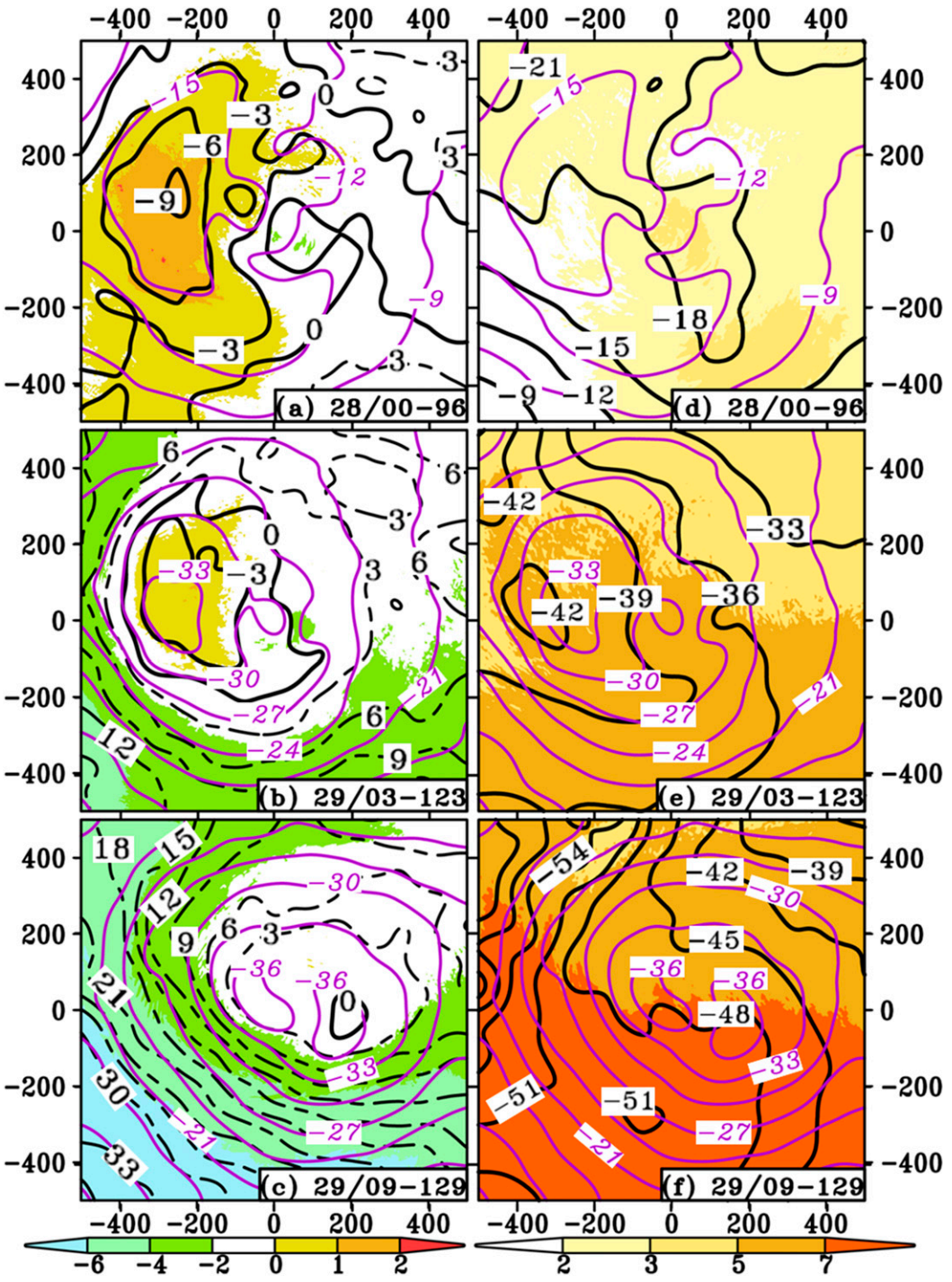

FIG. 12. (a)–(c) Horizontal distribution of the hydrostatically calculated total SLP changes (purple contours at 3-hPa intervals) and the hydrostatically calculated SLP changes (black contours at 3-hPa intervals; solid for negative, dotted for positive) associated with the mass-weighted TW changes (shaded, °C)—that is, in the layers below 12 km [the mass-weighted temperature changes are estimated by $\int \Delta T(x, y, p, t)\, dp / \int dp$, valid at 28/00-96, 29/03-123, and 29/09-129, respectively, from the WRF 1.667-km-resolution (1000 km × 1000 km) subdomain]. Both the temperature and SLP changes are calculated with respect to 26/16-64. (d)–(f) As in (a)–(c), respectively, but for the mass-weighted SW—that is, in the layers above 12 km. See text for more details.

regions at 29/09-129 is more than 6 K colder than that at 26/16-64 (Fig. 12c) and about 30 K less in θ_e than that at 28/00-96 (Figs. 6d–g). Much less cooling occurs in the core region owing to the presence of intense rotation, and over the cold northern regions, especially in the frontogenesis region. As a result, SLP rises of more than 35 hPa from that at 26/16-64 appear in the outer regions compared to little SLP changes in the core. From a mass–wind balance view, the resulting large radial SLP gradients and thermal gradients would superimpose pronounced tangential flows on the reference (26/16-64) flow field.

While SW_H induces larger SLP falls, its associated radial SLP gradients are smaller than those induced by TW_H, especially in the core region, as can be seen from the density of their falling-SLP isobars. Only at 29/09–129, large falling-SLP gradients occur in the western semicircle as a result of the approaching of the cold front (cf. Figs. 12f and 6g,n). In general, SW_H causes SLP falls across the storm from the west to east, which generates asymmetries in horizontal winds, thereby expanding Sandy's lower pressure coverage and associated cyclonic circulation, as shown in section 4a. In contrast, negative TW_H and its cyclonic advection account for larger (much less) SLP increases over the warm southern (cold northern) regions and frontogenetic forcing in the northeastern quadrant, respectively. Nevertheless, despite the large SW_H-induced SLP falls, it is still TW_H and its associated dynamical processes that are responsible for a sizeable amount of the intensity changes of rotational winds and the size expansion, especially at later stages.

d. Inner-core vertical structures

So far, we have examined the vertical thermal structures with respect to two different reference times. When they are plotted with respect to the storm environment (Figs. 13b–d), the lower-stratospheric warmth is no longer visible because of the rapid overspread of the lower-stratospheric air across the storm. This appears to explain why the impact of the lower-stratospheric warmth on Sandy's large SLP falls was not noted by the previous studies of the case.

Figure 13a shows that the RI stage is characterized by nearly symmetric eyewall structures with a typical in–up–out secondary circulation. Note the development of double warm cores: a typical midtropospheric one of greater than 6°C located at $z = 4$ km (Zhang et al. 2000) and a lower-stratospheric one of more than 2°C at $z = 16$ km. The latter is not related to the horizontal advection of the lower-stratospheric warm air from the west but the descent of lower-stratospheric air above associated with convective bursts (Chen and Zhang 2013); it diminishes rapidly after entering the weakening stage, as also shown in Figs. 8, 9a, and 9b. As VWS increases, wavenumber-1 convective asymmetry becomes more evident. The TC vortex, together with its warm column (Fig. 13b), tilts to the downshear left (Reasor et al. 2004; Davis et al. 2008b), so the vertical cross section is taken along a line that is 45°–60° rotated to the left of the VWS vector (see Figs. 3 and 6). Similarly, lower-level inflows and upper-level outflows are no longer symmetric (i.e., with a low-level inflow and an upper-level outflow on the downshear left and a reversed flow configuration on the upshear right); they are similar to those observed and simulated in sheared TCs—for example, Hurricanes Olivia and Jimena (Black et al. 2002) and Bonnie (Zhu et al. 2004). In particular, a deep inflow layer (i.e., $z = 2$–12 km) of lower-θ_e air occurs on the upshear right with some cloud hydrometeors, and an upper-cloud mass (i.e., above $z = 8$ km), where rotational flows (and inertial stability) are weak (cf. Figs. 9b and 13b), intrudes into the eye center, thereby diminishing warm columns above through evaporative cooling of cloud hydrometeors. As a result, P_{MIN} rises notably as it is mainly associated with a warm column in the lowest 6 km (cf. Figs. 13b, 3a, and 6i).

The steady-V_{MAX} stage is seen with weakening convection in the partial eyewall and much reduced warm-core intensity (cf. Figs. 13c and 6d). Little eyewall characteristics are present on the upshear side where deep convection is suppressed. In spite of the weakening warm core, the SLP fields keeps dropping (cf. Figs. 3a, 7a, and 8) as a result of the previously mentioned advection of stratospheric warm air, which can be seen from the lowering tropopause height from $z = 16$ to 14 km (cf. Figs. 13b and 13c). The tropopause height falls farther to $z = 12$–13 km after entering the reintensification stage, in which a robust midlevel warm core redevelops together with enhanced deep convection in the northwestern quadrant of the partial eyewall (Fig. 13d). The level of the peak warmth occurs near $z = 5$ km, which is similar to the satellite-observed warm core of Sandy by Zhu and Weng (2013). This warm core can be seen being more associated with compensating subsidence that is peaked near the top of the eyewall convection where inertial stability is weak. Note that the eyewall convection could only reach as high as 11 km, which is 4–5 km lower than that occurred earlier (cf. Figs. 13a–d), as has also been shown in Fig. 9. Note also the development of a deep outflow layer below 6 km and weak inflows above on the upshear side of the storm, where deep convection is suppressed owing to the presence of intense VWS. This lower-tropospheric outflow is not a typical feature of mature TCs, and it is associated with the southeastern portion of the frontal

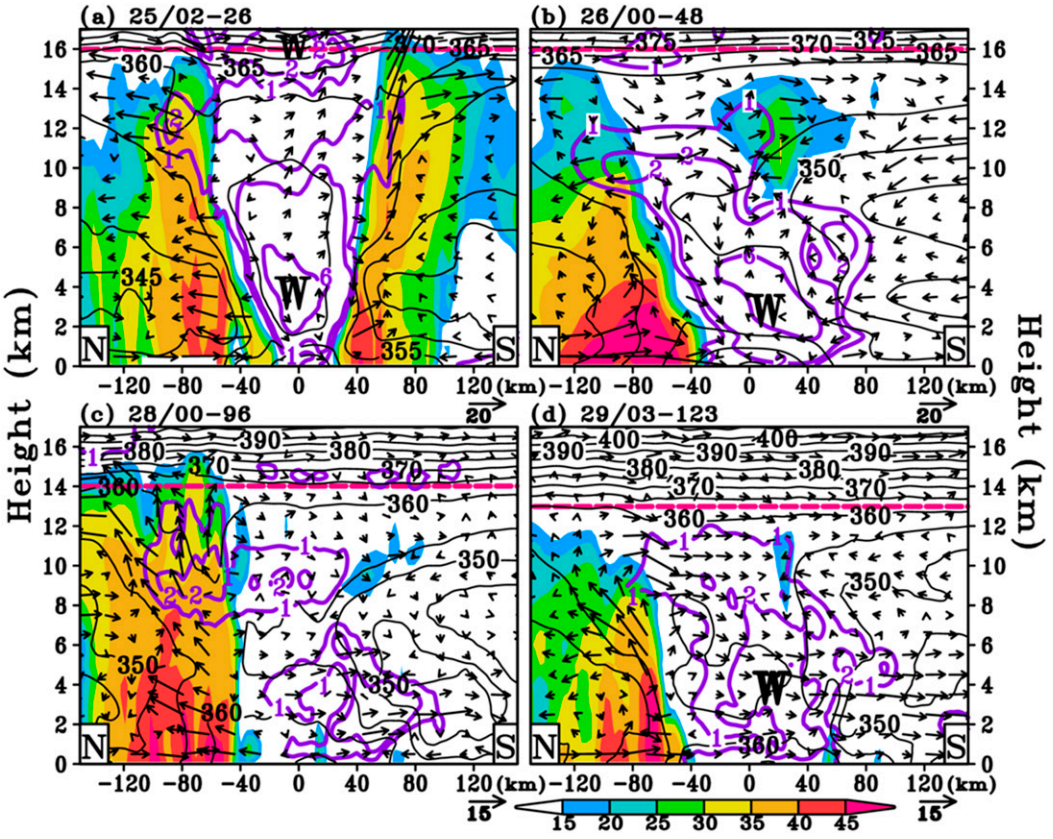

FIG. 13. Vertical cross section of the simulated radar reflectivity (shaded, dBZ), equivalent potential temperature θ_e at 5-K intervals, temperature deviations from the corresponding level-averaged value (purple contours at 1, 2, and 6 K), and storm-relative in-plane flow vectors (with vertical velocity multiplied by 5) from the 1.667-km-resolution domain at (a) 25/02-26, (b) 26/00-48, (c) 28/00-96, and (d) 29/03-123 along line NS (through the vortex center) given in Fig. 6. The tropopause height (defined in Fig. 8) is denoted by dashed magenta lines. Horizontal axis indicates the distance (km) from the storm center. Letter "W" indicates the warm-core center.

rainband (cf. Figs. 13d and 6f). Its development tends to weaken inner-core rotation, at least locally, because of the unfavorable AAM transport (Yau et al. 2004). Instead, two jets take place on the right and left region outside the cross section (i.e., near R = 200 km; see Figs. 6m,n), respectively, as mentioned before.

5. Summary and conclusions

In this study, the relative importance of moist frontogenesis and tropopause undulation in determining the multiple intensity, size, and structural changes of Hurricane Sandy is examined using a 138-h (0000 UTC 24 October–1800 UTC 29 October 2012) cloud-resolving version of the WRF Model. Results show that the WRF Model reproduces Sandy's life cycle consisting of four distinct development stages: (i) rapid intensification, (ii) weakening, (iii) steady V_{MAX} but with large SLP falls, and (iv) reintensification prior to landfall. Typical correlations between Sandy's intensity changes and SST and VWS are found during the first two stages. A time–height cross-sectional analysis reveals that the large SLP falls during the steady-V_{MAX} and subsequent reintensification stages result from Sandy's moving into lower-tropopause regions associated with an eastward-propagating MT, where the associated lower-stratospheric warm air is advected across the storm with higher PV wrapped into the core region. Despite the large SLP falls in Sandy's core and ambient regions, we do not see significant increases in PGF$_R$, and so little changes in the peak rotational wind during the steady-V_{MAX} stage, even in the presence of frontal rainbands in the outer region.

Results also show that Sandy's northward movement over cooler water toward a zonally distributed baroclinic zone associated with an eastern Canadian high increases meridional θ_e gradients in the northern semicircle. As a result, three spiral frontogenetic zone/rainbands develop successively in the northeastern quadrant from the weakening to reintensification stage, where Sandy's

high-θ_e southeasterly flow converges with a low-θ_e easterly flow in the northern environment. They are then advected northwestward by the intense easterly flow. Cyclonical inward advection of AAM along each spiral frontal rainband tends to produce a local jet streak, mainly in the outer northeastern quadrant. This appears to account for Sandy's continued expansion of the tropical storm–force wind and structural changes. However, warm frontogenesis contributes little to Sandy's inner-core intensity changes (i.e., in V_{MAX}) during the weakening and steady-V_{MAX} stages. The merging of the final two frontogenetic zones/rainbands and the partial eyewall convection into a spiral intensifying frontal rainband results in a much enhanced spiral jet extending from its core (i.e., V_{MAX}) in the southwestern quadrant to the outer northeastern quadrant during the final stage. Results suggest that the frontogenetically produced wind streaks during the weakening and steady-V_{MAX} stages tend to precondition the outer regions and then contribute to Sandy's reintensification through the cyclonic inward advection of the associated AAM. It is this cyclonic inward progression of the jet core (also implying contraction) along the spiral frontal rainband and eyewall leads to the reintensification of the storm. Meanwhile, cyclonic advection of the low-θ_e (cold) air into Sandy's southern semicircle increases radial thermal contrasts and SLP gradients, thus generating and maintaining a (balanced) swirling jet in its southern sectors. Although some of the above results remain to be validated by high-resolution observations in the future, our work shows several interesting features related to the ET of TCs that have not been previously shown: (i) steady V_{MAX} with pronounced P_{MIN} falls; (ii) multiple warm-frontogenesis events within Sandy's internal circulation, and their different roles during its different stages; (iii) the important roles of the lower-stratospheric warmth in generating widespread SLP falls, but with little impact on the inner-core maximum rotational wind speed of the storm; and (iv) reintensification prior to a warm seclusion due mostly to Sandy's vortex dynamics interacting with the frontogenetically produced wind streaks.

In conclusion, we may state that it is mainly (i) the moist frontogenesis processes resulting from the convergence of Sandy's high-θ_e southeasterly flows with low-θ_e easterly flows from the northern environment that lead to the continued size expansion and structural changes and (ii) the merged frontogenetic zones/rainbands and partial eyewall convection, and the subsequent cyclonic inward contraction of a well-developed jet core along the merged rainband that account for Sandy's reintensification. The lower-stratospheric warmth makes large contributions to P_{MIN} and environmental SLP falls, and likely size expansion during the final stage, and it appears to play a role in modulating Sandy's structural and intensity changes. In a forthcoming study, the size expansion and intensity changes as related to Sandy's outflow dynamics during the final stage will be examined.

Acknowledgments. This work was supported by ONR Grant N000141410143 and NASA Grant NNX12AJ78G. The WRF Model integration was performed on the Discover machine of NASA Center for Climate Simulation (NCCS). The Gridded Satellite (GridSat-B1) data, developed by Knapp et al. (2011) of NOAA CDR Program, was downloaded from National Climatic Data Center (http://www.ncdc.noaa.gov). We wish to thank Prof. Hyeong-Bin Cheong and Mr. Hyun-Gyu Kang of Pukyong National University, South Korea, and Dr. In-Hyuk Kwon of the Korea Institute of Atmospheric Prediction Systems, South Korea, for providing the advanced bogussing algorithm code for the present study.

REFERENCES

Atallah, E., and L. F. Bosart, 2003: The extratropical transition and precipitation distribution of Hurricane Floyd (1999). *Mon. Wea. Rev.*, **131**, 1063–1081, doi:10.1175/1520-0493(2003)131<1063:TETAPD>2.0.CO;2.

Black, M. L., J. F. Gamache, F. D. Marks, C. E. Samsury, and H. E. Willoughby, 2002: Eastern Pacific Hurricanes Jimena of 1991 and Olivia of 1994: The effect of vertical shear on structure and intensity. *Mon. Wea. Rev.*, **130**, 2291–2312, doi:10.1175/1520-0493(2002)130<2291:EPHJOA>2.0.CO;2.

Blake, E. S., T. B. Kimberlain, R. J. Berg, J. P. Cangialosi, and J. L. Beven II, 2013: Tropical cyclone report: Hurricane Sandy (AL18222012). National Hurricane Center, 157 pp. [Available online at http://www.nhc.noaa.gov/2012atlan.shtml.]

Bosart, L. F., and G. M. Lackmann, 1995: Postlandfall tropical cyclone reintensification in a weakly baroclinic environment: A case study of Hurricane David (September 1979). *Mon. Wea. Rev.*, **123**, 3268–3291, doi:10.1175/1520-0493(1995)123<3268:PTCRIA>2.0.CO;2.

Browning, K. A., G. Vaughan, and P. Panagi, 1998: Analysis of an ex-tropical cyclone after reintensifying as a warm-core extratropical cyclone. *Quart. J. Roy. Meteor. Soc.*, **124**, 2329–2356, doi:10.1002/qj.49712455108.

Cecelski, F. S., and D.-L. Zhang, 2013: Genesis of Hurricane Julia (2010) within an African easterly wave: Low-level vortices and upper-level warming. *J. Atmos. Sci.*, **70**, 3799–3817, doi:10.1175/JAS-D-13-043.1.

Chen, H., and D.-L. Zhang, 2013: On the rapid intensification of Hurricane Wilma (2005). Part II: Convective bursts and the upper-level warm core. *J. Atmos. Sci.*, **70**, 146–162, doi:10.1175/JAS-D-12-062.1.

Colle, B. A., 2003: Numerical simulations of the extratropical transition of Floyd (1999): Structural evolution and responsible mechanisms for the heavy rainfall over the northeast United States. *Mon. Wea. Rev.*, **131**, 2905–2926, doi:10.1175/1520-0493(2003)131<2905:NSOTET>2.0.CO;2.

Davis, C. A., and Coauthors, 2008a: Prediction of landfalling hurricanes with the Advanced Hurricane WRF Model. *Mon. Wea. Rev.*, **136**, 1990–2005, doi:10.1175/2007MWR2085.1.

——, S. C. Jones, and M. Riemer, 2008b: Hurricane vortex dynamics during Atlantic extratropical transition. *J. Atmos. Sci.*, **65**, 714–736, doi:10.1175/2007JAS2488.1.

Donelan, M. A., B. K. Haus, N. Reul, W. J. Plant, M. Stiassnie, H. C. Graber, O. B. Brown, and E. S. Saltzman, 2004: On the limiting aerodynamic roughness of the ocean in very strong winds. *Geophys. Res. Lett.*, **31**, L18306, doi:10.1029/2004GL019460.

Dudhia, J., 1989: Numerical study of convection observed during the winter monsoon experiment using a mesoscale two-dimensional model. *J. Atmos. Sci.*, **46**, 3077–3107, doi:10.1175/1520-0469(1989)046<3077:NSOCOD>2.0.CO;2.

Evans, C., and R. E. Hart, 2008: Analysis of the wind field evolution associated with the extratropical transition of Bonnie (1998). *Mon. Wea. Rev.*, **136**, 2047–2065, doi:10.1175/2007MWR2051.1.

Evans, J. L., and R. E. Hart, 2003: Objective indicators of the life cycle evolution of extratropical transition for Atlantic tropical cyclones. *Mon. Wea. Rev.*, **131**, 909–925, doi:10.1175/1520-0493(2003)131<0909:OIOTLC>2.0.CO;2.

Galarneau, T. J., C. A. Davis, and M. A. Shapiro, 2013: Intensification of Hurricane Sandy (2012) through extratropical warm core seclusion. *Mon. Wea. Rev.*, **141**, 4296–4321, doi:10.1175/MWR-D-13-00181.1.

Harr, P. A., and R. L. Elsberry, 2000: Extratropical transition of tropical cyclones over the western North Pacific. Part I: Evolution of structural characteristics during the transition process. *Mon. Wea. Rev.*, **128**, 2613–2633, doi:10.1175/1520-0493(2000)128<2613:ETOTCO>2.0.CO;2.

Hill, K. A., and G. M. Lackmann, 2009: Influence of environmental humidity on tropical cyclone size. *Mon. Wea. Rev.*, **137**, 3294–3315, doi:10.1175/2009MWR2679.1.

Hirschberg, P. A., and J. M. Fritsch, 1991a: Tropopause undulations and the development of extratropical cyclones. Part I: Overview and observations from a cyclone event. *Mon. Wea. Rev.*, **119**, 496–517, doi:10.1175/1520-0493(1991)119<0496:TUATDO>2.0.CO;2.

——, and ——, 1991b: Tropopause undulations and the development of extratropical cyclones. Part II: Diagnostic analysis and conceptual model. *Mon. Wea. Rev.*, **119**, 518–550, doi:10.1175/1520-0493(1991)119<0518:TUATDO>2.0.CO;2.

Hong, S.-Y., and J.-O. J. Lim, 2006: The WRF single-moment 6-class microphysics scheme (WSM6). *J. Korean Meteor. Soc.*, **42**, 129–151.

——, J. Dudhia, and S.-H. Chen, 2004: A revised approach to ice microphysical processes for the bulk parameterization of clouds and precipitation. *Mon. Wea. Rev.*, **132**, 103–120, doi:10.1175/1520-0493(2004)132<0103:ARATIM>2.0.CO;2.

——, Y. Noh, and J. Dudhia, 2006: A new vertical diffusion package with an explicit treatment of entrainment processes. *Mon. Wea. Rev.*, **134**, 2318–2341, doi:10.1175/MWR3199.1.

Jones, S. C., and Coauthors, 2003: The extratropical transition of tropical cyclones: Forecast challenges, current understanding, and future directions. *Wea. Forecasting*, **18**, 1052–1092, doi:10.1175/1520-0434(2003)018<1052:TETOTC>2.0.CO;2.

Kain, J. S., 2004: The Kain–Fritsch convective parameterization: An update. *J. Appl. Meteor.*, **43**, 170–181, doi:10.1175/1520-0450(2004)043<0170:TKCPAU>2.0.CO;2.

Kaplan, J., and M. DeMaria, 2003: Large-scale characteristics of rapidly intensifying tropical cyclones in the North Atlantic basin. *Wea. Forecasting*, **18**, 1093–1108, doi:10.1175/1520-0434(2003)018<1093:LCORIT>2.0.CO;2.

Keyser, D., M. J. Reeder, and R. J. Reed, 1988: A generalization of Petterssen's frontogenesis function and its relation to the forcing of vertical motion. *Mon. Wea. Rev.*, **116**, 762–780, doi:10.1175/1520-0493(1988)116<0762:AGOPFF>2.0.CO;2.

Klein, P. M., P. A. Harr, and R. L. Elsberry, 2000: Extratropical transition of Western North Pacific tropical cyclones: An overview and conceptual model of the transformation stage. *Wea. Forecasting*, **15**, 373–395, doi:10.1175/1520-0434(2000)015<0373:ETOTWNP>2.0.CO;2.

Knapp, K. R., and Coauthors, 2011: Globally gridded satellite observations for climate studies. *Bull. Amer. Meteor. Soc.*, **92**, 893–907, doi:10.1175/2011BAMS3039.1.

Kwon, I.-H., and H.-B. Cheong, 2010: Tropical cyclone initialization with a spherical high-order filter and an idealized three-dimensional bogus vortex. *Mon. Wea. Rev.*, **138**, 1344–1367, doi:10.1175/2009MWR2943.1.

Lackmann, G. M., 2015: Hurricane Sandy before 1900 and after 2100. *Bull. Amer. Meteor. Soc.*, **96**, 547–560, doi:10.1175/BAMS-D-14-00123.1.

Liu, Y., D.-L. Zhang, and M. K. Yau, 1999: A multiscale numerical study of Hurricane Andrew (1992). Part II: Kinematics and inner-core structures. *Mon. Wea. Rev.*, **127**, 2597–2616, doi:10.1175/1520-0493(1999)127<2597:AMNSOH>2.0.CO;2.

Magnusson, L., J.-R. Bidlot, S. T. K. Lang, A. Thorpe, and N. Wedi, 2014: Evaluation of medium-range forecasts of Hurricane Sandy. *Mon. Wea. Rev.*, **142**, 1962–1981, doi:10.1175/MWR-D-13-00228.1.

Mlawer, E. J., S. J. Taubman, P. D. Brown, M. J. Iacono, and S. A. Clough, 1997: Radiative transfer for inhomogeneous atmospheres: RRTM, a validated correlated-*k* model for the longwave. *J. Geophys. Res.*, **102**, 16 663–16 682, doi:10.1029/97JD00237.

Neuman, S., and J. G. Boyd, 1962: Hurricane movement and variable location of high intensity spot in wall cloud radar echo. *Mon. Wea. Rev.*, **90**, 371–374, doi:10.1175/1520-0493(1962)090<0371:HMAVLO>2.0.CO;2.

Powell, M. D., S. H. Houston, L. R. Amat, and N. Morisseau-Leroy, 1998: The HRD real-time hurricane wind analysis system. *J. Wind Eng. Ind. Aerodyn.*, **77–78**, 53–64.

Reasor, P. D., M. T. Montgomery, and L. D. Grasso, 2004: A new look at the problem of tropical cyclones in vertical shear flow: Vortex resiliency. *J. Atmos. Sci.*, **61**, 3–22, doi:10.1175/1520-0469(2004)061<0003:ANLATP>2.0.CO;2.

Ritchie, E. A., and R. L. Elsberry, 2007: Simulations of the extratropical transition of tropical cyclones: Phasing between the upper-level trough and tropical cyclones. *Mon. Wea. Rev.*, **135**, 862–876, doi:10.1175/MWR3303.1.

Shapiro, M. A., and D. Keyser, 1990: Fronts, jet streams, and the tropopause. *Extratropical Cyclones: The Erik Palmén Memorial Volume*, C. W. Newton and E. O. Holopainen, Eds., Amer. Meteor. Soc., 167–191.

Skamarock, W. C., and Coauthors, 2008: A description of the Advanced Research WRF version 3. NCAR Tech. Note NCAR/TN-475+STR, 113 pp., doi:10.5065/D68S4MVH.

Thorncroft, C. D., and S. C. Jones, 2000: The extratropical transitions of Hurricanes Felix and Iris in 1995. *Mon. Wea. Rev.*, **128**, 947–972, doi:10.1175/1520-0493(2000)128<0947:TETOHF>2.0.CO;2.

Velden, C., 1992: Satellite-based microwave observations of tropopause-level thermal anomalies: Qualitative

application in extratropical cyclone events. *Wea. Forecasting*, **7**, 669–682, doi:10.1175/1520-0434(1992)007<0669:SBMOOT>2.0.CO;2.

Wang, Y., 2009: How do outer spiral rainbands affect tropical cyclone structure and intensity? *J. Atmos. Sci.*, **66**, 1250–1273, doi:10.1175/2008JAS2737.1.

Yau, M. K., Y. Liu, D.-L. Zhang, and Y. Chen, 2004: A multiscale numerical study of Hurricane Andrew (1992). Part VI: Small-scale inner-core structures and wind streaks. *Mon. Wea. Rev.*, **132**, 1410–1433, doi:10.1175/1520-0493(2004)132<1410:AMNSOH>2.0.CO;2.

Zhang, D.-L., and H. Chen, 2012: Importance of the upper-level warm core in the rapid intensification of a tropical cyclone. *Geophys. Res. Lett.*, **39**, L02806, doi:10.1029/2011GL050578.

——, and L. Zhu, 2012: Roles of upper-level processes in tropical cyclogenesis. *Geophys. Res. Lett.*, **39**, L17804, doi:10.1029/2012GL053140.

——, Y. Liu, and M. K. Yau, 2000: A multiscale numerical study of Hurricane Andrew (1992). Part III: Dynamically induced vertical motion. *Mon. Wea. Rev.*, **128**, 3772–3788, doi:10.1175/1520-0493(2001)129<3772:AMNSOH>2.0.CO;2.

Zhu, T., and F. Weng, 2013: Hurricane Sandy warm-core structure observed from advanced Technology Microwave Sounder. *Geophys. Res. Lett.*, **40**, 3325–3330, doi:10.1002/grl.50626.

——, D.-L. Zhang, and F. Weng, 2004: Numerical simulation of Hurricane Bonnie (1998). Part I: Eyewall evolution and intensity changes. *Mon. Wea. Rev.*, **132**, 225–241, doi:10.1175/1520-0493(2004)132<0225:NSOHBP>2.0.CO;2.